Journal of Thermal Analysis and Calorimetry
https://doi.org/10.1007/s10973-026-15578-1

Application of neural network analysis to study thermally stratified hybrid nanofluid over a variable thickness sheet

Hussan Zeb[1] · Mdi Begum Jeelani[2] · Kamal Shah[3] · Zeeshan Ali[4] · Manar A. Alqudah[5] · Aiman Mukheimer[3] · Thabet Abdeljawad[1,3,6]

Received: 14 March 2026 / Accepted: 24 April 2026

Abstract

Enhancing the efficiency of thermal systems requires advanced working fluids with superior heat transfer characteristics. In this study, we investigate the thermally stratified magnetohydrodynamic (MHD) flow of a TiO_2–Fe_3O_4/H_2O hybrid nanofluid over a nonlinear stretching sheet with variable thickness. The model incorporates temperature-dependent viscosity and thermal conductivity, thermal radiation, internal heat generation, and a non-Fourier heat flux based on the Cattaneo–Christov theory. The governing partial differential equations are transformed into a system of coupled nonlinear ordinary differential equations using appropriate similarity transformations. These equations are solved numerically using a shooting method combined with a Runge–Kutta scheme. Moreover, an artificial neural network (ANN) model is created based on the Levenberg–Marquardt algorithm to estimate velocity and temperature profiles as a surrogate model. ANN performance is measured by statistical measures of error such as mean squared error (MSE), root-mean-square error (RMSE) and regression coefficient (R), and it is found that they are in excellent agreement with the numerical results. Parametric study indicates that an increase in the magnetic parameter (M) decreases the velocity of the object considerably because of the Lorentz force and increases the temperature field. Temperature decreases as Prandtl number (Pr) and thermal stratification parameter (St) increase, and this means that the thermal diffusion is lower. The heat transfer rate increases with radiation parameter (R) and convective parameter (B_1). The results demonstrate that the hybrid nanofluid enhances heat transfer performance compared to single nanofluids, and the proposed ANN model provides an efficient predictive tool for complex nonlinear thermal systems.

Keywords Thermally stratified flow · Hybrid nanofluid TiO_2 and Fe_3O_4 · Generalized Fourier's law · Inclined magnetic field · Neural network (NN) analysis

List of Symbols

A	Stretching rate constant (dimensionless)
B_0	Magnetic field strength (T)
$\Bumpeq_2$	Temperature-dependent viscosity parameter (dimensionless)

✉ Thabet Abdeljawad
tabdeljawad@psu.edu.sa

Hussan Zeb
zebhussan5@gmail.com

Mdi Begum Jeelani
mbshaikh@imamu.edu.sa

Kamal Shah
kshah@psu.edu.sa

Zeeshan Ali
zeeshan@yuntech.edu.tw

Manar A. Alqudah
maalqudah@pnu.edu.sa

Aiman Mukheimer
mukheimer@psu.edu.sa

[1] Department of Fundamental Sciences, Faculty of Engineering and Architecture, Istanbul Gelisim University, 34310 Avcilar, Istanbul, Turkey

[2] Department of Mathematics and Statistics, College of Science, Imam Mohammad Ibn Saud Islamic University (IMSIU), Riyadh, Saudi Arabia

[3] Department of Mathematics and Sciences, Prince Sultan University, 11586 Riyadh, Saudi Arabia

[4] Department of Information Management, National Yunlin University of Science and Technology, 123 University Road, Section 3, Douliou, Yunlin 64002, Taiwan R.O.C.

[5] Department of Mathematical Sciences, College of Science, Princess Nourah bint Abdulrahman University, P.O. Box 84428, 11671 Riyadh, Saudi Arabia

[6] Department of Medical Research, China Medical University, Taichung 40402, Taiwan

$\Bumpeq_3$ Wall thickness parameter (dimensionless)
b_1, b_2 Temperature coefficients in viscosity/conductivity models
C_f Skin friction coefficient (dimensionless)
M Magnetic parameter (dimensionless), $M = \frac{\sigma B_0^2}{\rho U_0}$
m Stretching index (dimensionless)
q Heat flux vector (W m^{-2})
N_u The Nusselt number (dimensionless)
Pr The Prandtl number $\mathrm{Pr} = \frac{\mu C_p}{k}$
Q_1, Q_2 Heat source parameters
R Thermal radiation parameter (dimensionless)
q_w Wall heat flux (W m^{-2})
T Temperature (K)
St Parameter due to thermal stratification (dimensionless), $\mathrm{St} = \frac{n_2}{n_1}$
T_w Wall temperature (K)
T_0 Reference temperature (K)
T_∞ Ambient temperature (K)
u, v Velocity components (m s^{-1})
u_w Stretching sheet velocity $u_w = U_0(x + d)^{m-1}(\frac{m}{s})$

Greek symbols

α_1 Inclination angle of magnetic field (rad)
Γ Thermal relaxation time (s)
ζ Similarity variable
θ Dimensionless temperature, $\theta = \frac{T-T_\infty}{T_w-T_\infty}$
λ_1 Thermal conductivity variation parameter (dimensionless)
λ_2 Thermal relaxation parameter, $\lambda_2 = \Gamma U_0(c + x)^{m-1}$
μ_{hnf} Unit of viscosity (kgm s^{-2})
ρ_{hnf} Density (kg m^{-3})
σ_{hnf} Electrical conductivity $\frac{S}{s}$
ϕ_1, ϕ_2 Volume fractions of Fe_3O_4 and TiO_2 nanoparticles

Abbreviations and Acronyms

ANN Artificial Neural Network
BLMM Back Propagation Levenberg–Marquardt
BVP Boundary Value Problem
LM Levenberg–Marquardt
MHD Magnetohydrodynamics
MSE Mean Square Error
RK45 Runge–Kutta 4th/5th-order method

Introduction

Numerous engineering fields, such as heat exchangers, fuel cells, and fluid-based thermal systems, rely heavily on efficient heat transfer phenomena. However, the fact that traditional fluids have low thermal conductivity makes it imperative to come up with specialized fluids that have high thermal conductivities to address this issue. A concept that was introduced by Choi et al. [1] is that of nanofluids; base fluids with suspended nanometer-sized particles, which are much more effective thermal conductors than traditional fluids. Therefore, various scholars have studied heat transfer in flowing nanofluid at various physical conditions. To further enhance thermal performance, hybrid nanofluids concept has been derived using two types of nanoparticles.

The application of hybrid nanoparticles can be done in a variety of applications including heat exchangers, solar energy systems, HVAC applications, automotive cooling, power generation turbines, electronic thermal management, biotechnology and power plants. A magnetic field was investigated by Zeb et al. [2] on a rotating surface to the hybrid nanofluid flow and reported improved heat transfer performance of hybrid nanoscale materials synthesized through the incorporation of three distinct nanoparticles in a base fluid in Obalalu et al. [3]. This strategy proves very effective in enhancing thermal conductivity than binary hybrid nanofluids. They are highly applicable in solar energy applications, industrial heat exchangers, microelectronic cooling, and biomedical applications including hypothermia therapy and targeted drug delivery, although the high cost of production, long-term stability, and possible toxicity of nanoparticles continue to be the subject of research. Thus, the hybrid nanofluid technology has a bright future of enhancing energy efficiency and in the sphere of medical use. Bhatti et al. [4] examined the use of hybrid nanofluids to use silicon dioxide (SiO_2) nanoparticles in solar energy systems. Nabwey et al. [5, 6] came up with mathematical models of ternary hybrid nanofluids in solar energy applications. Zeb et al. [7] studied the effect of the internal energy on melting heat transfer in ternary hybrid nanofluids in coaxial disk to disk. Also, Zeb et al. [8] suggested the application of ternary hybrid nanoparticles in the modified system of heat flux in rotating disk systems.

The ANN scheme is the most capable method for determining nonlinear flow problems when using different geometries to drive the designing progresses. An ANN scheme for fluid problems is one of the development goals. This progression will enhance the efficiency of thermal control framework, which can be applied to innovative concepts to energize sustainable using less energy for alternative engineering fields. This area present as an ideal platform for applying computational solution, especially when it is considered to be advantageous to heat transfer performance thermodynamics in complex fluid systems, aerospace engineering and other manufacturing procedure. Such systems may be applicable to the development of more efficient heat exchanges and pumps to enhance fluid flows in lubrication, cooling, and chemical processes. ANN can be applied to new input scenarios to predict thermal patterns, velocities, other flow parameters after training and testing. Bar et al. [9] predicted the compressible flow of a non-Newtonian fluid on using an (ANN) through a pipe comprising its parts. Zhao et al. [10] used neural network to analyze the impacts of entropy generation on Ree–Eyring fluid model through a rotatable disk. Alizadeh et al. [11] have been presented mix-convection flow of heat transfer in a non-Newtonian nanofluid by using an (ANN) methods through an enclosed cavity.

Heat transfer analysis is a essential field because it is widely used in chemical processing, petroleum engineering, and biological systems (e.g., drug delivery and heat transfer in organs). The conventional Fourier law was developed by Fourier in 1822 to describe the heat conduction in different experiments. The thermophysical characteristics of the liquid metals in the temperature range of 0–400 °C are reported by Yu et al. [12]. The energy equation created by Fourier suggests instant propagation of thermal disturbances through a medium. To overcome this shortcoming, Cattaneo et al. proposed a revised constitutive relation that included thermal relaxation, and the energy equation was became hyperbolic Cattaneo et al. [13]. This model was further refined by Christov et al. [14] who used the upper-convected derivatives introduced by Oldroyd to make it frame-indifferent. Fourier transform is considered as classical in theory although it possesses weaknesses when it comes to explaining transient thermal processes. This has given rise to non-Fourier models such as the Cattaneo–Christov theory which has been used in modern engineering systems [15, 16]. The recent experimentation of the impact of thermal relaxation has revealed that they play a significant role in microscale heat transfer and biology [17, 18].

Owing to temperature variations in fluids, density variations develop leading to a phenomenon known as thermal stratification. Natural systems, such as the atmosphere, lakes, and oceans, have stratified layers, which play a role in determining thermal efficiency by inhibiting convectional mixing and minimizing vertical heat transfer. The Richardson number commonly measures the strength of stratification and is the buoyancy force ration to the shear of the flows. In this case, both mass and heat transfer processes co-occur, resulting in complementary temperature gradients, and this is known as double stratification. Stratification is also widely used in industrial applications, in the environment (e.g., salinity stratification in estuaries and thermal stratification in lakes) and engineering (e.g., power-plant condensers and underground storage tanks). Recently, the influence of thermal stratified flow on a Maxwell fluid in heat transfer analysis through an exponential sheet has been investigated [19]. Noor et al. [20] studied temperature-dependent stratification in ferrofluids in the presence of a stretching sheet owing to the influence of a magnetic dipole. Chen calculated natural convection on stratified flow through a stretching surface using a finite-difference scheme [21]. Daniel et al. [19] simulated the thermally stratified with magnetohydrodynamic nanofluid flow with viscous dissipation. Thermal stratification remains a subject of interest because of its contribution to energy efficiency in industrial and environmental processes. Modern studies have focused on the optimization of stratified systems to use them in renewable power applications and thermal storage [22, 23]. The occurrence of double stratification has been widely observed in nanofluid systems, and recent observations suggest that its ability to improve heat transfer performance significantly improved through this phenomenon [24, 25]. Phase change materials have been studied using the Cattaneo–Christov theory, which has created new opportunities in storage of thermal energy available in the future [26]. Heat exchangers and cooling applications in stratified flow in electrical microchannels were investigated in [27, 28].

In modern studies of heat transfer flows, the simplifying hypothesis of constant fluid viscosity and thermal conductivity is gradually being replaced by models in which they are inherently temperature dependent. A combination of these variable properties can significantly change the expected hydrodynamic and thermal boundary layers qualified for constant-property simulations, as demonstrated in recent high-reliability numerical experiments. This dependence can be characterized accurately with the help of modern experimental methods, where Shah et al. [29] showed a 38% change in the effective thermal conductivity of Al_2O_2-CuO/water hybrid nanofluids in a 50 K working range, which is effectively modeled by a linear temperature dependence. This method is based on initial studies such as Chiam [30], who combined variable conductivity with heat sources dependent on temperature. On the same note, the effect of the change in thermal viscosity on the patterns of convection is an imperative area of concern. Recent particle image velocity research by Chen [31] demonstrated the effect of a 40 percent reduction in the viscosity of a silicone-based nanofluid on the reorganization of vortex structures in the natural convection of a magnetite heated sphere and the continuity of the analysis of Molla et al. [32]. Currently, it is common to combine several coupled phenomena in this study. An example of this is a computational model of the laminar flow over a catalytic plate that simultaneously accounts for variable viscosity, chemical reaction kinetics, and an isotropic mass diffusion, as developed by Kumar et al. [33] as an extension of the previous framework of Ghaly [34]. Recently, Abbas et al. [43] studied numerical investigation of a fluid problem. Zeb et al. [44] studied Cattaneo-Christov heat flux model. Maatki et al. [45] have used ANN to investigate fluid problem. Wahab [46] has studied a slip boundaray value problem for numerical analysis. Awan et al. [47] studied entropy optimization in MHD hybrid nanofluid flow.

In the literature review, it is noted that there is a deep gap in research related to the modeling of the thermally stratified hybrid nanofluid flow with the inclusion of the non-Fourier heat transfer mechanisms across the nonlinear stretching surfaces. In particular, the combined effects of variable thermophysical properties, Cattaneo–Christov heat flux, and inclined magnetohydrodynamic (MHD) forces have not been investigated within a unified framework. Most of the available literature, however, does not consider thermal stratification or non-Fourier heat flux, as well as variable thermophysical properties, simultaneously. Moreover, ANN-based methods are frequently used without strict validation or incorporating with complex physical models. A dual computational approach of the shooting method with RK45 integration is used to solve the resulting boundary value problem. Moreover, an artificial neural network (ANN) model is developed which is a rapid, dependable, and data-intensive surrogate to validation and parametric forecasting. The findings give informative details on the dynamics of velocity and temperature distributions in the flow field. In addition, important engineering quantities such as the skin friction coefficient and Nusselt number are evaluated. Altogether, this article fills the research gap between the theoretical fluid mechanics and practical thermal engineering by offering a more coherent and comprehensive framework of hybrid nanofluid-based thermal management systems.

Research gap and objectives

Research gap

An extensive review of the available literature indicates that significant progress has been made in modeling nanofluid and hybrid nanofluid flows under various physical effects such as magnetohydrodynamics, thermal radiation, and nonlinear stretching surfaces. However, several important aspects remain insufficiently addressed.

- First, most existing studies consider either constant thermophysical properties or only partially account for temperature-dependent viscosity and thermal conductivity. The combined influence of both variable viscosity and variable thermal conductivity in hybrid nanofluids is still limited in the literature.
- Second, although the Cattaneo–Christov heat flux model has been widely used to describe non-Fourier heat conduction, its integration with thermally stratified hybrid nanofluid flow over a variable thickness nonlinear stretching surface has not been fully explored.
- Third, the simultaneous effects of inclined magnetic fields, internal heat generation, thermal radiation, and convective boundary conditions in a unified hybrid nanofluid model are rarely investigated in a single framework.
- Furthermore, while artificial neural networks (ANNs) have been applied to fluid-flow problems, their use as surrogate models for validating complex hybrid nanofluid systems involving non-Fourier heat flux and stratification remains scarce. Therefore, there exists a clear research gap in developing a comprehensive mathematical and computational framework that incorporates all these coupled physical mechanisms while also employing machine learning techniques for validation and prediction.

Objectives of the study

To address the identified research gaps, the main objectives of the present study are as follows:

- To develop a mathematical model for thermally stratified magnetohydrodynamic flow of a TiO_2–Fe_3O_4/H_2O hybrid nanofluid over a nonlinear stretching surface with variable thickness.
- To incorporate temperature-dependent viscosity and thermal conductivity along with the Cattaneo–Christov non-Fourier heat flux model in the governing equations.
- To model the overall effects of inclined magnetic field, thermal radiation, internal heat generation, and convective boundary conditions in a single model.
- To reduce the governing partial differential equations to a system of nonlinear ordinary differential equations by the use of suitable similarity transformations.
- To find the correct numerical solutions of the resulting BVP by shooting method coupled with the RK45 integration scheme.
- To create and train an artificial neural network (ANN) model as a proxy tool to predict velocity and temperature profiles and check the numerical findings.
- To determine the relationship between the influence of the important physical parameters on the velocity, temperature, skin friction coefficient, and heat transfer rate.
- To provide physical insight and practical guidance for the design of advanced thermal systems involving hybrid nanofluids in engineering applications such as solar energy systems, cooling technologies, and thermal management devices.

Problem description and assumptions

This study considers the steady two-dimensional thermally stratified magnetohydrodynamic (MHD) flow of a hybrid nanofluid consisting of TiO_2 and Fe_3O_4 nanoparticles suspended in water over a stretching sheet of variable thickness. The model models a number of significant physical influences, which are: an inclined magnetic field, Cattaneo–Christov heat flux, thermal radiation, heat production/absorption, temperature-sensitive thermal conduction/viscosity. The stretching velocity follows a power-law distribution

$$u_{\mathrm{w}}(x) = U_0(c+x)^{\mathrm{m}},$$

where U_0 is the reference stretching velocity, c is a dimensional constant introduced to avoid singularity at $x = 0$, and m is the nonlinear stretching index. The surface profile is defined as

$$y = A(c+x)^{\frac{1-\mathrm{m}}{2}},$$

where A denotes the sheet-thickness coefficient. A uniform magnetic field B_0 is applied at an angle α_1 $(0 < \alpha_1 < \pi/2)$ relative to the surface plane, as displayed in Fig. 1.

Following Refs. [35–37], the mathematical model for thermally stratified hybrid nanofluid flow with Cattaneo–Christov heat flux is written as follows. The continuity equation is

$$\nabla \cdot \bar{\mathbf{V}} = 0. \tag{1}$$

The momentum equation is

$$\rho_{\mathrm{hnf}}\left(\frac{\partial \bar{\mathbf{V}}}{\partial t} + (\bar{\mathbf{V}} \cdot \nabla)\bar{\mathbf{V}}\right) = \nabla \cdot (-p\mathbf{I} + \boldsymbol{\tau}) + \mathbf{F} - \sigma_{\mathrm{hnf}} B_0^2 \sin^2(\alpha_1)\bar{\mathbf{V}}, \tag{2}$$

where

$$\boldsymbol{\tau} = \mu_{\mathrm{hnf}}(T)\left(\nabla\bar{\mathbf{V}} + (\nabla\bar{\mathbf{V}})^T\right), \qquad \mathbf{F} = -\sigma_{\mathrm{hnf}} B_0^2 \sin^2(\alpha_1)\bar{\mathbf{V}}. \tag{3}$$

Here, $\mathbf{F}$ represents the magnetic body force, B_0 is the magnetic field strength, σ_{hnf} is the electrical conductivity of the hybrid nanofluid, and α_1 is the inclination angle of the applied magnetic field.

Using the standard boundary layer approximations, the continuity and momentum equations reduce to

$$\frac{\partial u}{\partial x} + \frac{\partial v}{\partial y} = 0, \tag{4}$$

$$\frac{\rho_{\mathrm{hnf}}}{\rho_{\mathrm{f}}}\left(u\frac{\partial u}{\partial x} + v\frac{\partial u}{\partial y}\right) = \frac{\partial}{\partial y}\left(\frac{\mu_{\mathrm{hnf}}}{\mu_{\mathrm{f}}}(T)\frac{\partial u}{\partial y}\right) - \frac{\sigma_{\mathrm{hnf}} B_0^2 \sin^2(\alpha_1)}{\sigma_{\mathrm{f}}}u. \tag{5}$$

The energy equation based on the Cattaneo–Christov model is given by

$$(\rho C_{\mathrm{p}})_{\mathrm{hnf}}\left(\frac{\partial T}{\partial t} + (\bar{\mathbf{V}} \cdot \nabla)T\right) = -\nabla \cdot \bar{\mathbf{q}}, \tag{6}$$

where u and v denote the velocity components in the x- and y-directions, respectively, T is the fluid temperature, C_{p} is the specific heat capacity, and $\bar{\mathbf{q}}$ is the heat flux vector satisfying

$$\bar{\mathbf{q}} + \Gamma\left[\frac{\partial \bar{\mathbf{q}}}{\partial t} + (\nabla \cdot \bar{\mathbf{V}})\bar{\mathbf{q}} + \bar{\mathbf{V}} \cdot \nabla\bar{\mathbf{q}} - \bar{\mathbf{q}} \cdot \nabla\bar{\mathbf{V}}\right] = -\frac{k_{\mathrm{hnf}}}{k_{\mathrm{f}}}(T)\nabla T, \tag{7}$$

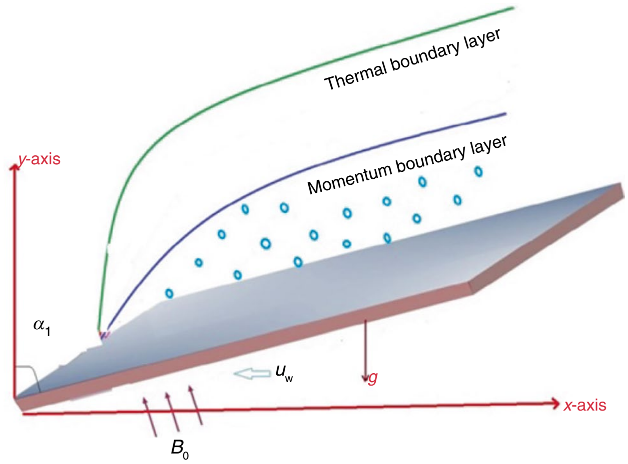

Fig. 1 The geometric configuration of the problem

where Γ is the thermal relaxation time and $k_{\mathrm{hnf}}(T)$ denotes the temperature-dependent thermal conductivity of the hybrid nanofluid. For an incompressible hybrid nanofluid, Eq. (7) reduces to

$$\bar{\mathbf{q}} + \Gamma\left[\frac{\partial \bar{\mathbf{q}}}{\partial t} + \bar{\mathbf{V}} \cdot \nabla\bar{\mathbf{q}} - \bar{\mathbf{q}} \cdot \nabla\bar{\mathbf{V}}\right] = -\frac{k_{\mathrm{hnf}}}{k_{\mathrm{f}}}(T)\nabla T. \tag{8}$$

Eliminating the heat flux vector $\bar{\mathbf{q}}$ from Eqs. (6) and (8) yields the governing energy equation in the following form:

$$\begin{aligned}\frac{(\rho C_{\mathrm{p}})_{\mathrm{hnf}}}{(\rho C_{\mathrm{p}})_{\mathrm{f}}}\left(v\frac{\partial T}{\partial y} + u\frac{\partial T}{\partial x}\right) &= \frac{\partial}{\partial y}\left(k_{\mathrm{hnf}}(T)\frac{\partial T}{\partial y}\right)\\ &+ Q_{\mathrm{S}}(T_{\mathrm{w}} - T_\infty)e^{n\xi_2} + \frac{16\gamma_{\mathrm{sb}}T_\infty^3}{3\gamma_{\mathrm{ma}}}\frac{\partial^2 T}{\partial y^2}\\ &- Q_{\mathrm{T}}(T_{\mathrm{w}} - T) - \Gamma\left(v^2\frac{\partial^2 T}{\partial y^2} + u\frac{\partial T}{\partial x}\frac{\partial u}{\partial x} + u\frac{\partial T}{\partial y}\frac{\partial v}{\partial x}\right.\\ &\left.+ v\frac{\partial T}{\partial y}\frac{\partial v}{\partial y} + v\frac{\partial T}{\partial x}\frac{\partial u}{\partial y} + 2vu\frac{\partial^2 T}{\partial x \partial y} + u^2\frac{\partial^2 T}{\partial x^2}\right).\end{aligned} \tag{9}$$

Here, γ_{ma} and γ_{sb} denote the mean absorption coefficient and Stefan–Boltzmann constant, respectively, whereas Q_{S} and Q_{T} are the heat source parameters.

The corresponding boundary conditions are

$$\begin{cases} u(x,y) = u_{\mathrm{w}}(x) = U_0(c+x)^{\mathrm{m}}, \quad v(x,y) = 0, & \text{at } y = A(c+x)^{\frac{1-\mathrm{m}}{2}},\\ \dfrac{k_{\mathrm{hnf}}(T)}{k_{\mathrm{f}}}\dfrac{\partial T}{\partial y} = -h_{\mathrm{f}}(T_{\mathrm{w}} - T), & \text{at } y = A(c+x)^{\frac{1-\mathrm{m}}{2}},\\ u(x,y) \to 0, \quad T \to T_\infty, & \text{as } y \to \infty. \end{cases} \tag{10}$$

In the above formulation, T_{w} is the variable wall temperature, T_∞ is the ambient temperature, and thermal stratification is incorporated through the temperature boundary conditions.

Following Refs. [37–39], the dimensionless temperature and variable-property relations are defined as

$$\begin{aligned}\theta(\eta) &= \frac{T-T_\infty}{T_w-T_0},\\ \frac{\mu_{hnf}(T)}{\mu_f} &= \mu_0\frac{a-b_1(T-T_w)}{(1-\phi_2)^{2.5}(1-\phi_1)^{2.5}},\\ \frac{k_{hnf}(T)}{k_f} &= k_0\frac{k_{hnf}}{k_f}\big(a_1-b_2(T_\infty-T)\big).\end{aligned}\tag{11}$$

The following similarity transformations reduce the governing PDE system to a system of nonlinear ODEs:

$$\eta=\sqrt{\frac{(1+m)U_0}{2\nu}}\,y\,(x+c)^{\frac{m-1}{2}},\qquad \psi=\left[\sqrt{\frac{2U_0\nu}{m+1}}\,G(\xi)\right](c+x)^{\frac{m+1}{2}},\tag{12}$$

$$\begin{aligned}u &= U_0(c+x)^m G'(\xi),\\ v &= -\left(\frac{(m+1)\nu U_0}{2}\right)^{\frac{1}{2}}\left[G(\xi)+\xi\frac{m-1}{m+1}G'(\xi)\right](x+c)^{\frac{m-1}{2}},\end{aligned}\tag{13}$$

$$\Theta(\xi)=\frac{T-T_\infty}{T_w-T_0},\tag{14}$$

where the wall and ambient temperatures vary according to

$$T_w=T_0+k_1(x+c)^{\frac{1-m}{2}},\qquad T_\infty=T_0+k_2(x+c)^{\frac{1-m}{2}}.\tag{15}$$

Hence, the dimensional temperature can be written as

$$T=T_\infty+\Theta\,(T_w-T_\infty).\tag{16}$$

The thermal stratification relations then become

$$b_1(T_w-T_0)=b_1k_1(c+x)^{\frac{1-m}{2}},\qquad b_1(T_\infty-T_0)=b_1k_2(c+x)^{\frac{1-m}{2}},\tag{17}$$

and consequently

$$b_1(T_w-T_0)=\zeta,\qquad b_1(T_\infty-T_0)=\zeta S_t,\qquad S_t=\frac{k_2}{k_1}.\tag{18}$$

Here, S_t is the thermal stratification parameter; λ_1 and λ_2 are the variable conductivity and thermal relaxation parameters, respectively; and μ_f and k_f are the viscosity and thermal conductivity of the base fluid. Using the above transformations, Eqs. (5)–(9) reduce to the following coupled ODE system:

$$\begin{aligned}&\frac{\mu_{hnf}}{\mu_f}\left[\big(\eqsim_1+\eqsim_2(1-\Theta-St)\big)F'''-\eqsim_2\Theta'F''\right]\\ &\quad+2m\frac{\rho_{hnf}}{\rho_f}\left(\frac{(F')^2}{m+1}-F'F\right)\\ &\quad-\frac{2M}{m+1}\frac{\sigma_{hnf}}{\sigma_f}\sin^2(\alpha_1)F'=0,\end{aligned}\tag{19}$$

$$\begin{aligned}&\frac{k_{hnf}}{k_f\mathrm{Pr}}\left[(\eqsim_1+\lambda_1\Theta)\Theta''+\lambda_1(\Theta')^2\right]\\ &\quad+\frac{\lambda_2}{2}\frac{(\rho C_p)_{hnf}}{(\rho C_p)_f}\left(\frac{2}{\lambda_2}\Theta'F+(m-3)F'F-(m-1)\Theta''F^2\right)\\ &\quad+Q_1e^{-2.5n}+Q_2\Theta+S_t\left(\frac{m-1}{1+m}\right)F'=0.\end{aligned}\tag{20}$$

The corresponding boundary conditions are

$$\begin{cases}F(0)=\eqsim_3\dfrac{1-m}{1+m},\qquad F'(0)=1,\\ \Theta'(0)=-B_1\left(\dfrac{1-\Theta(0)}{\big(\lambda_1\Theta(0)+\eqsim_1\big)k_{hnf}/k_f}\right),\\ F'(\infty)=0,\qquad \Theta(\infty)=0.\end{cases}\tag{21}$$

For notational convenience, let $F(\zeta)=g(\zeta)$ and $\Theta(\zeta)=\theta(\zeta)$. Then, the transformed governing equations can be written as

$$\frac{\mu_{hnf}}{\mu_f}\left[\big(\eqsim_1+\eqsim_2(1-S_t-\theta)\big)g'''-\eqsim_2\theta'g''\right]+\frac{\rho_{hnf}}{\rho_f}\left(g'g-\frac{2m}{m+1}(g')^2\right)-\frac{2M}{m+1}\frac{\sigma_{hnf}}{\sigma_f}\sin^2(\alpha_1)g'=0,\tag{22}$$

$$\begin{aligned}&\frac{1}{\mathrm{Pr}}\left[R+\frac{k_{hnf}}{k_f}\big(\lambda_1\theta+\eqsim_1\big)\theta''+\lambda_1\frac{k_{hnf}}{k_f}(\theta')^2\right]-S_t\left(\frac{1-m}{m+1}\right)g'\\ &\quad+\frac{\lambda_2}{2}\frac{(\rho C_p)_{hnf}}{(\rho C_p)_f}\left(\frac{2}{\lambda_2}\theta'g+(m-3)g'g-(m-1)\theta''g^2\right)+Q_2\theta+Q_1e^{-2.5n}=0,\end{aligned}\tag{23}$$

with boundary conditions

$$\begin{cases} g(0) = \backsimeq_3 \dfrac{1-m}{m+1}, \qquad g'(0) = 1, \\ \theta'(0) = -B_1\left(\dfrac{1-\theta(0)}{\left(\lambda_1\theta(0) + \backsimeq_1\right)k_{\mathrm{hnf}}/k_{\mathrm{f}}}\right), \\ g'(\infty) = 0, \qquad \theta(\infty) = 0. \end{cases} \tag{24}$$

Here, $g'(\zeta)$ and $\theta(\zeta)$ denote the dimensionless velocity and temperature, respectively. The parameter $\backsimeq_3 = A\sqrt{\frac{U_0(m+1)}{2\nu}}$ is the wall thickness parameter, $M = \frac{\sigma B_0^2}{\rho U_0 (c+x)^{\mathrm{m}-1}}$ is the magnetic parameter, $\lambda_2 = U_0\Gamma(c+x)^{\mathrm{m}-1}$ is the thermal relaxation parameter, $\mathrm{Pr} = \mu C_{\mathrm{p}}/k_\infty$ is the Prandtl number, and Q_1 and Q_2 are the heat source parameters.

Table 1 Thermophysical properties of TiO_2, Fe_3O_4, and water [8, 40]

Property	TiO_2	Fe_3O_4	H_2O
$\rho/\ \mathrm{kg\,m^{-3}}$	4250	5180	997.1
$C_{\mathrm{p}}/\ \mathrm{J\,kg^{-1}K^{-1}}$	686.2	650	4180.0
$k\ \ /\mathrm{W\,m^{-1}K^{-1}}$	8.9538	9.7	0.6071
$\sigma\ \ /\mathrm{S\,m^{-1}}$	2.6×10^6	0.74×10^7	0.05

Thermal and transport properties of hybrid nanofluid

In the present study, the hybrid nanofluid consists of TiO_2 and Fe_3O_4 nanoparticles dispersed in water as the base fluid. The effective thermophysical properties, including density, heat capacity, viscosity, thermal conductivity, and electrical conductivity, are modeled by standard mixture relations in terms of the nanoparticle volume fractions ϕ_1 and ϕ_2. This choice is consistent with the physical model and removes any ambiguity regarding the nanoparticle composition (Tables 1 and 2).

The engineering quantities of interest are the skin friction coefficient and the local Nusselt number, which characterize the wall shear stress and heat transfer rate, respectively. They are defined as

$$C_{\mathrm{f}} = \frac{\tau_{\mathrm{w}}}{\rho\sqrt{\frac{m+1}{2}}}, \qquad Nu = \frac{(x+b)\,q_{\mathrm{w}}}{k_{\mathrm{f}}\left(T_{\mathrm{w}} - T_\infty\right)\sqrt{\frac{m+1}{2}}}. \tag{25}$$

Here, τ_{w} denotes the wall shear stress and q_{w} is the wall heat flux, given by

$$\tau_{\mathrm{w}} = \left[\mu_{\mathrm{hnf}}(T)\,\frac{\partial u}{\partial y}\right]_{y=A(c+x)^{\frac{1-m}{2}}}, \tag{26}$$

$$q_{\mathrm{w}} = \left[-\frac{k_{\mathrm{hnf}}(T)}{k_{\mathrm{f}}}\,\frac{\partial T}{\partial y} - q_{\mathrm{r}}\right]_{y=A(x+c)^{\frac{1-m}{2}}}. \tag{27}$$

Their dimensionless forms are therefore expressed as

Table 2 Correlations used for the TiO_2–Fe_3O_4/H_2O hybrid nanofluid.

Property	Correlation
Viscosity (μ)	$\frac{\mu_{\mathrm{hnf}}}{\mu_{\mathrm{f}}} = \frac{1}{(1-\phi_2)^{5/2}(1-\phi_1)^{5/2}}.$
Density (ρ)	$\frac{\rho_{\mathrm{hnf}}}{\rho_{\mathrm{f}}} = (1-\phi_1)\left[(1-\phi_2) + \phi_2\frac{\rho_2}{\rho_{\mathrm{f}}}\right] + \phi_1\frac{\rho_1}{\rho_{\mathrm{f}}}.$
Heat capacity (ρC_{p})	$\frac{(\rho C_{\mathrm{p}})_{\mathrm{hnf}}}{(\rho C_{\mathrm{p}})_{\mathrm{f}}} = (1-\phi_1)\left[(1-\phi_2) + \phi_2\frac{(\rho C_{\mathrm{p}})_2}{(\rho C_{\mathrm{p}})_{\mathrm{f}}}\right] + \phi_1\frac{(\rho C_{\mathrm{p}})_1}{(\rho C_{\mathrm{p}})_{\mathrm{f}}}.$
Thermal conductivity (k)	$\frac{k_{\mathrm{nf}}}{k_{\mathrm{f}}} = \frac{2k_{\mathrm{f}} + k_1 - 2\phi_1(k_{\mathrm{f}} - k_1)}{2k_{\mathrm{f}} + k_1 + \phi_1(k_{\mathrm{f}} - k_1)},$ $\frac{k_{\mathrm{hnf}}}{k_{\mathrm{nf}}} = \frac{2k_{\mathrm{nf}} + k_2 - 2\phi_2(k_{\mathrm{nf}} - k_2)}{2k_{\mathrm{nf}} + k_2 + \phi_2(k_{\mathrm{nf}} - k_2)}.$
Electrical conductivity (σ)	$\frac{\sigma_{\mathrm{nf}}}{\sigma_{\mathrm{f}}} = 1 + \frac{3\left(\frac{\sigma_1}{\sigma_{\mathrm{f}}} - 1\right)\phi_1}{\left(\frac{\sigma_1}{\sigma_{\mathrm{f}}} + 2\right) - \left(\frac{\sigma_1}{\sigma_{\mathrm{f}}} - 1\right)\phi_1},$ $\frac{\sigma_{\mathrm{hnf}}}{\sigma_{\mathrm{nf}}} = 1 + \frac{3\left(\frac{\sigma_2}{\sigma_{\mathrm{nf}}} - 1\right)\phi_2}{\left(\frac{\sigma_2}{\sigma_{\mathrm{nf}}} + 2\right) - \left(\frac{\sigma_2}{\sigma_{\mathrm{nf}}} - 1\right)\phi_2}.$
Buoyancy coefficient ($\rho\beta$)	$\frac{(\rho\beta)_{\mathrm{hnf}}}{(\rho\beta)_{\mathrm{f}}} = (1-\phi_1)\left[(1-\phi_2) + \phi_2\frac{(\rho\beta)_2}{(\rho\beta)_{\mathrm{f}}}\right] + \phi_1\frac{(\rho\beta)_1}{(\rho\beta)_{\mathrm{f}}}.$

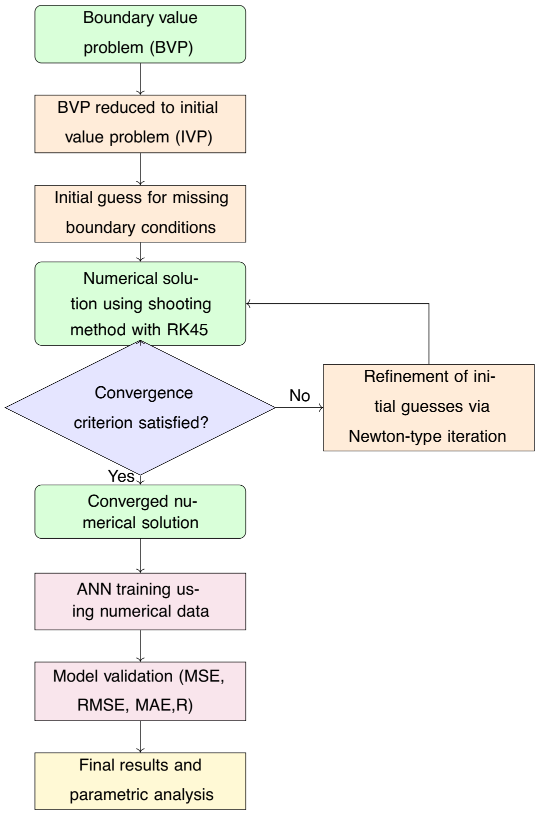

Fig. 2 Flowchart of the shooting technique with ANN validation

$$
\begin{aligned}
C_{\mathrm{f}} &= \frac{\mu_{\mathrm{hnf}}}{\mu_{\mathrm{f}}}\left(\bumpeq_1 + \bumpeq_2\bigl(1-(\theta+S_t)\bigr)\right)\sqrt{\frac{m+1}{2Re_{\mathrm{x}}}}\, g''(0),\\
\frac{Nu_{\mathrm{x}}}{\sqrt{Re_{\mathrm{x}}}} &= -\left[\frac{k_{\mathrm{hnf}}}{k_{\mathrm{f}}}\bigl(\lambda_1\theta + \bumpeq_1\bigr) + \frac{4}{3}R\right]\theta'(0).
\end{aligned}
\tag{28}
$$

Numerical approximation

See Fig. 2.

Shooting method

To solve the transformed boundary value problem, the coupled higher-order ordinary differential equations are first converted into an equivalent first-order system. This step facilitates the implementation of the shooting technique together with a Runge–Kutta integration scheme. Let

$$
g = y_1, \quad g' = y_2, \quad g'' = y_3, \quad \theta = y_4, \quad \theta' = y_5. \tag{29}
$$

With these substitutions, the governing system is rewritten as

$$
\begin{aligned}
y_1' &= y_2,\\
y_2' &= y_3,\\
y_3' &= \frac{\dfrac{\rho_{\mathrm{hnf}}}{\rho_{\mathrm{f}}}\left(y_1y_3 - \dfrac{2m}{m+1}y_2^2\right) - \dfrac{2M\sin^2(\alpha_1)}{m+1}\dfrac{\sigma_{\mathrm{hnf}}}{\sigma_{\mathrm{f}}}y_2 - \beta_2\dfrac{\mu_{\mathrm{hnf}}}{\mu_{\mathrm{f}}}y_3y_5}{\dfrac{\mu_{\mathrm{hnf}}}{\mu_{\mathrm{f}}}\bigl(\beta_1 + \beta_2(1 - y_4 - St)\bigr)},\\
y_4' &= y_5,\\
y_5' &= \Pr\frac{\dfrac{(\rho C_{\mathrm{p}})_{\mathrm{hnf}}}{(\rho C_{\mathrm{p}})_{\mathrm{f}}}\left(\dfrac{\lambda_2(m-3)}{2}y_1y_2 + St\dfrac{m-1}{m+1}y_2\right) + Q_2y_4 + Q_1e^{-2.5\mathrm{n}}}{\dfrac{k_{\mathrm{hnf}}}{k_{\mathrm{f}}}(\beta_1 + \lambda_1y_4) + \dfrac{\lambda_2\Pr(m+1)}{2}y_1^2 + \dfrac{4R}{3}}.
\end{aligned}
\tag{30}
$$

The associated boundary conditions become

$$
\begin{cases}
y_1(0) = \beta_3\dfrac{1-m}{m+1}, \qquad y_2(0) = 1,\\
y_5(0) = -B_1\left(\dfrac{1-y_4(0)}{(\lambda_1y_4(0)+\beta_1)k_{\mathrm{hnf}}/k_{\mathrm{f}}}\right),\\
y_2(\infty) = 0, \qquad y_4(\infty) = 0.
\end{cases}
\tag{31}
$$

Because the problem is posed as a boundary value problem, the unknown initial slopes are estimated iteratively using the shooting method. In this approach, the boundary value problem is transformed into an initial-value problem, and the missing initial conditions are adjusted until the far-field boundary conditions are satisfied. The resulting initial-value problem is solved numerically by the RK45 scheme. A step size of $h = 0.02$ and a convergence tolerance of 10^{-6} are used throughout the computations. Convergence is declared when the norm of the residual associated with the far-field boundary conditions falls below the prescribed tolerance.

This procedure provides stable and accurate numerical solutions for the velocity and temperature distributions and is used as the reference solution for subsequent ANN training and validation.

Artificial neural network (ANN)

The numerical solutions are represented by a trained artificial neural network (ANN) which is a Levenberg–Marquardt (LM) backpropagation algorithm. It is necessary to point out that the ANN is not implemented to substitute the numerical shooting-RK45 method, but it is an additional means of prediction, validation, and efficiency of the computations. This combination of numbers and ANN enhances reliability and offers a separate confirmation of the behavior of the solution.

The training sample is created using the numerical solutions of the shooting method with the RK45 integration framework. It considers a very large variety of governing physical parameters, among them the magnetic parameter, M, Prandtl number, Pr, thermal stratification parameter, St, thermal conductivity parameter, and thermal relaxation parameter, radiation parameter, and convective parameter, all denoted by their respective parameters. An ANN dataset is constructed by computing the profile of velocity, g', and temperature, theta, of each admissible parameter set, and using them to build the ANN dataset.

The ANN structure includes one hidden layer comprising of ten neurons that is chosen as a trade-off between computation and prediction efficiency. Levenberg–Marquardt algorithm is chosen because it converges quickly, and it is good in nonlinear function approximation problems with moderate size datasets.

This paper will detail the training and validation process of the ANN model. The ANN training and validation process is summarized as follows to make the process clear and reproducible:

- Data Generation: Numerical solutions are obtained in a structured grid of physical parameters by the shooting-RK45 method.
- **Input–Output Definition:** The input vector is given as.

  $[\eta, M, \Pr, \mathrm{St}, \lambda_1, \lambda_2, B_1, R]$,

  and the output vector is.

  $[g'(\eta), \theta(\eta)]$.

- **Data Normalization:** Minmax scaling is used to normalize all the input and output data:

  $$x_{\text{norm}} = \frac{x - x_{\min}}{x_{\max} - x_{\min}},$$

  to improve numerical stability and training.
- **Data Division:** The dataset is broken down into three subsets to have proper training and reliable evaluation of the model. In particular, 70% of the data is used on training the neural network, 15% for the validation to track the learning process and avoid overfitting, and the rest 15 percent is reserved to testing to evaluate the ability of the trained model to generalize.
- **Training Process:** The optimization algorithm to be used to train the network is the Levenberg–Marquardt algorithm that minimizes the mean squared error (MSE) between the predicted and target outputs. The algorithmic part of the training process continually modifies masses and biases according to the gradient information. item Early Stopping Criterion: To avoid overfitting, early stopping is implemented. Training will be stopped when the error in validation does not reduce after a specified number of iterations. item Tests and Generalization: The trained model is tested with unknown test data in order to test its generalization ability.

The ANN works on the following principle.

The network output of a normal neuron may be given as:

$$y_i = \mathcal{W}(b_i + w_i x_i), \tag{32}$$

in which x_i is the input, w_i is the connection mass, and b_i is the bias and is the activation function.

In forward propagation, the input data are sent across the hidden and output layers to produce predictions. With backpropagation, one propagates the prediction error backward to train masses and biases with gradient descent:

$$\frac{\partial L}{\partial w} = \frac{\partial L}{\partial y_j} \cdot \frac{\partial y_j}{\partial w}, \tag{33}$$

$$w_{\text{new}} = w_{\text{old}} - \eta \frac{\partial L}{\partial w}, \tag{34}$$

with the learning rate being denoted as, eta.

The predictive performance of the ANN model is evaluated using several statistical error measures, including the correlation coefficient R, mean squared error (MSE), root-mean-squared error (RMSE), and mean absolute error (MAE). These are measures that measure the difference between the ANN estimates and the numerical solutions. The expressions are given as follows:

$$R = \frac{n\sum XY - \sum X \sum Y}{\sqrt{\left[n\sum X^2 - (\sum X)^2\right]\left[n\sum Y^2 - (\sum Y)^2\right]}}. \tag{35}$$

$$\mathrm{MSE} = \frac{1}{N}\sum_{i=1}^{N}(y_i^{\mathrm{ANN}} - y_i^{\mathrm{num}})^2, \tag{36}$$

$$\mathrm{RMSE} = \sqrt{\frac{1}{N}\sum_{i=1}^{N}(y_i^{\mathrm{ANN}} - y_i^{\mathrm{num}})^2}, \tag{37}$$

$$\mathrm{MAE} = \frac{1}{N}\sum_{i=1}^{N}\left|y_i^{\mathrm{ANN}} - y_i^{\mathrm{num}}\right|. \tag{38}$$

Here, y_i^{ANN} and y_i^{num} represent the ANN-predicted and numerically obtained values, respectively, and N denotes the total number of data samples. Lower values of MSE, RMSE, and MAE indicate higher prediction accuracy, while a value of R close to unity signifies a strong agreement between the ANN outputs and the numerical results.

The quality of the trained ANN model is represented in various diagnostic plots in Figs. 3a–e and 4a–e, where each subfigure gives a particular understanding of the accuracy, convergence, and reliability of the network. The regression plots of Fig. 3d indicate the great consistency between

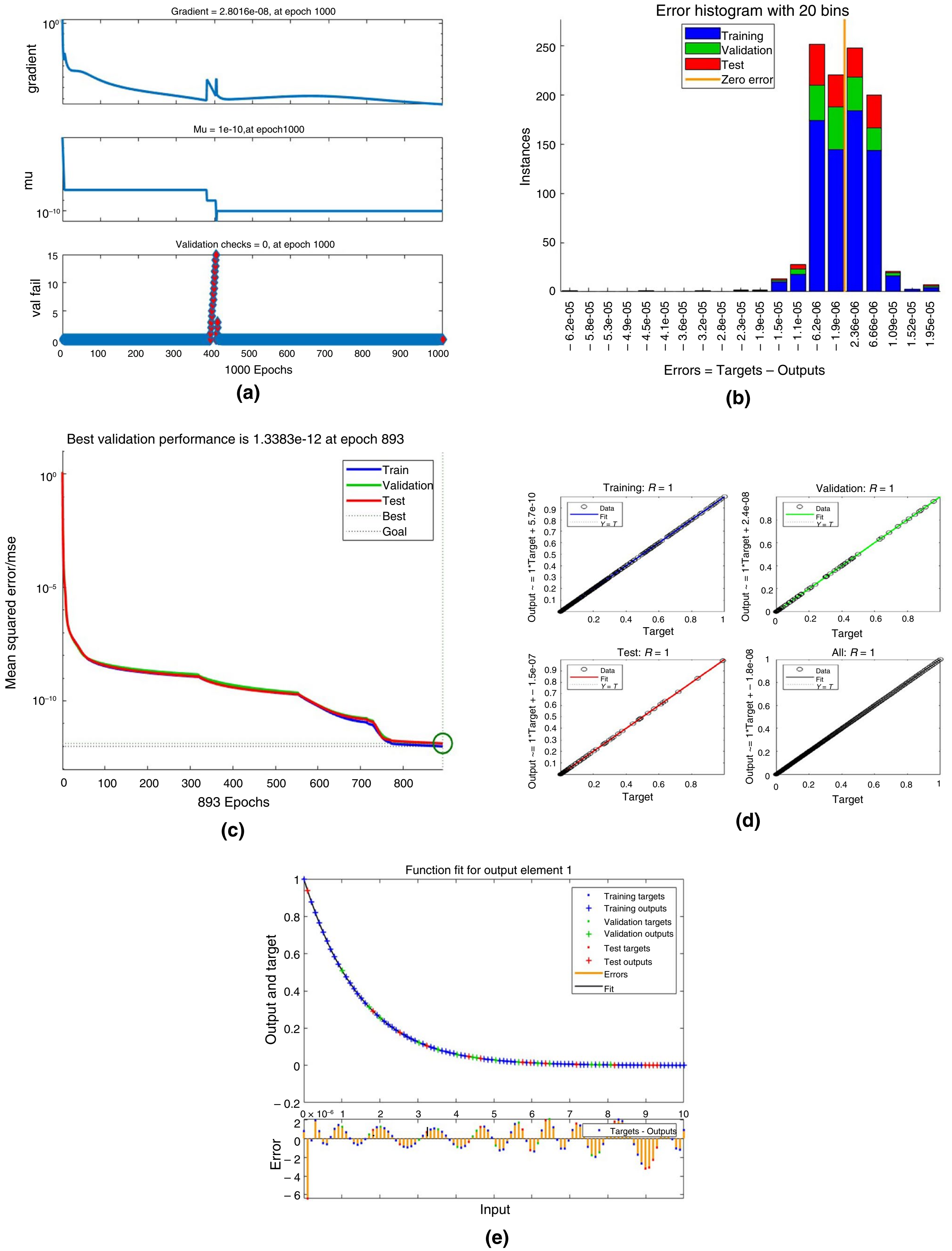

Fig. 3 The regression analysis, error histogram, performance plots, and curved fitting

the ANN predictions and the numerical solutions, and the regression coefficient is near to unity in the three training, validation, and testing sets, which shows high predictive power. The error histogram in Fig. 4b indicates that the errors of prediction are concentrated close to zero, which proves that the model is not biased and very accurate. In addition, as depicted in Fig. 3c, the performance curve indicates a sharp decrease in the mean squared error (MSE) at the early part of the training process and then the convergence is stabilized, which is a sign of successful network convergence without overfitting. Along with that, Fig. 4a shows the gradient and the evolution of the mu that were gradually decreasing, which indicates the stable convergence and the adaptive damping parameter is used to guarantee the efficient learning. The function fitting plot in Fig. 4e has an almost perfect overlap between ANN predictions and numerical results, which proves the model capacity to accurately reflect the nonlinear nature of the velocity and temperature fields.

Stability and convergence analysis

Tables 3 and 4 show how the numerical scheme is stable to changes in initial guesses and solver tolerances. It is seen that the highest deviations in the velocity profile and temperature profile are at most of the order of 10^{-5}. This is to confirm that the proposed shooting-RK45 method is stable, robust, and not sensitive to moderate changes in numerical parameters.

Validation and error analysis

The accuracy of the numerical and ANN results is validated through comparison with previously published studies and through quantitative error analysis. Table 5 presents the comparison of the present results with literature values, showing excellent agreement with very small absolute errors. In addition, the predictive capability of the ANN model is evaluated using RMSE and MAE, which are found to be of the order of 10^{-4}, indicating high accuracy. The regression coefficient R is found to be very near to unity which validates the fact of strong correlation of predicted and numerical results.

Results and discussion

This section gives a comprehensive examination of the computation findings of the shooting-ANN solution of the boundary layer flow of a hybrid of (TiO_2 and Fe_3O_4) nanofluid over a nonlinear stretching surface with thermal stratification. A shooting method combined with an ANN is used to find the numerical solutions of the boundary value problem represented by the equations in the form of the following equations (Eqs. (30)–(31) by setting the step size, h, to 0.02 and the convergence tolerance, TOL, to 10^{-5}. The numerical scheme was validated by comparison with previous literature [41, 42], and the results are analyzed in tabulated form and found to be in good agreement. The effect of the different parameters on the velocity and temperature fields is graphically studied in Figs. 5–21, and also, the heat transport rate and drag coefficient are analyzed in Tables 6–7.

Velocity profile

Figures 5–9 illustrate the impact of inclined magnetic parameter α_1 wall thickness parameter ß_2, thermal stratified parameter St parameters and thickness parameter ß_3, and magnetic M.

Figure 5 illustrates the effect of the wall thickness parameter ß_3 on the velocity profile for TiO_2 and Fe_3O_4 nanoparticles. It is observed that increasing ß_3 enhances the effective thickness of the stretching sheet, which intensifies the stretching action on the fluid. Consequently, the velocity of the fluid close to the wall rises and the velocity gradient becomes steeper and the momentum boundary layer thinness diminishes.

Figure 6 illustrates the effect of the thermal fluid property parameter $\eqcirc_2$ on the velocity gradient for TiO_2 and Fe_3O_4 nanoparticles. It is observed that increasing $\eqcirc_2$ reduces the velocity gradient. This is the case since an increase in values of $\eqcirc_2$ will increase the temperature dependence of viscosity and thus effective viscosity will increase as one goes close to the heated wall. The viscous resistance that ensues acts against fluid motion, thus slows down the flow velocity, and increases the momentum boundary layer.

Figure 7 illustrates the effect of the magnetic parameter M on the velocity profile $g'(\zeta)$ for both Fe_3O_4 and TiO_2 nanoparticles. It is observed that increasing M reduces the fluid velocity. This action can be explained by the Lorentz force created by the interaction between the electrically conducting fluid and the applied magnetic field which is also a resistive force against the flow. As a result, the flow velocity is slowed down, and the momentum boundary layer becomes thickened. Moreover, the damping effect is more pronounced for Fe_3O_4 nanoparticles due to their higher electrical conductivity compared to TiO_2, resulting in stronger magnetic resistance.

Figure 8 illustrates the effect of the stretching index parameter m on the velocity distribution for both Fe_3O_4 and TiO_2-based nanofluids. It is observed that the velocity decreases with increasing m. Physically, the parameter m governs the nonlinear stretching of the surface. The parameter, physically, m controls the nonlinear stretching of the

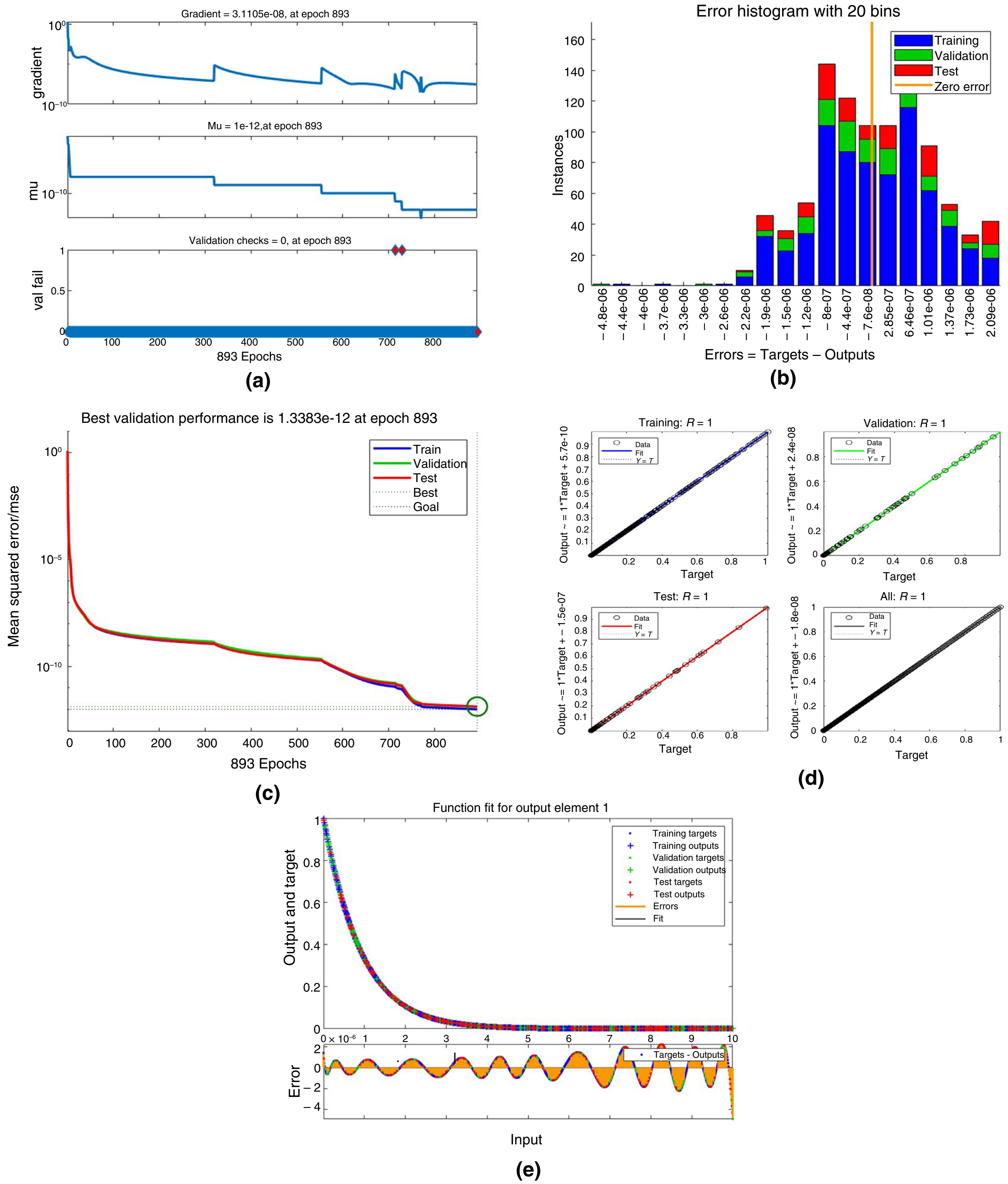

Fig. 4 The regression analysis, error histogram, performance plots, and curved fitting

surface. At the case of $m = 1$, the stretching velocity is linear and the case of $m \neq 1$ is nonlinear and changes the velocity gradient at the wall. Higher values of m weaken the effective fluid acceleration, resulting in reduced velocity and an increase in the momentum boundary layer thickness.

Table 3 Stability analysis with respect to different initial guesses

Case	$g''(0)$	$\theta(0)$	Max error in $g'(\eta)$	Max error in $\theta(\eta)$
1	−0.42351	0.31245	1.25×10^{-5}	9.87×10^{-6}
2	−0.42188	0.31092	1.12×10^{-5}	8.65×10^{-6}
3	−0.42230	0.31110	9.54×10^{-6}	7.82×10^{-6}

Table 4 Stability analysis with respect to solver tolerances

Case	RelTol	AbsTol	$g''(0)$	Max error in $g'(\eta)$	Max error in $\theta(\eta)$
1	10^{-4}	10^{-6}	−0.42320	2.14×10^{-5}	1.98×10^{-5}
2	10^{-5}	10^{-7}	−0.42240	1.12×10^{-5}	9.21×10^{-6}
3	10^{-6}	10^{-8}	−0.42205	7.80×10^{-6}	6.90×10^{-6}

Table 5 Validation of the present results with recent literature for selected values of the magnetic parameter M

M	Present	Awan et al. [41]	Absolute error	ANN	ANN Error
0.0	1.23254	1.23110	1.44×10^{-3}	1.23210	4.40×10^{-4}
0.4	1.19832	1.19725	1.07×10^{-3}	1.19801	3.10×10^{-4}
0.8	1.14567	1.14480	8.70×10^{-4}	1.14520	4.70×10^{-4}
1.2	1.08954	1.08860	9.40×10^{-4}	1.08901	5.30×10^{-4}

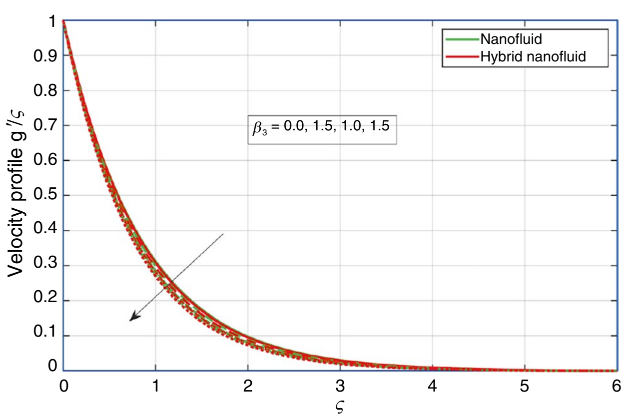

Fig. 5 Velocity impacts for thickness parameter β_3

Figure 9 illustrates the effect of the inclination angle α_1 on the velocity field for both Fe_3O_4 and TiO_2 nanoparticles. It is observed that the velocity decreases with increasing α_1. Physically, an increased inclination angle increases the effective part of the magnetic field on the fluid which increases Lorentz force. This resistant force resists the fluid motion, which results in a decrease in velocity and the increase in the momentum boundary layer.

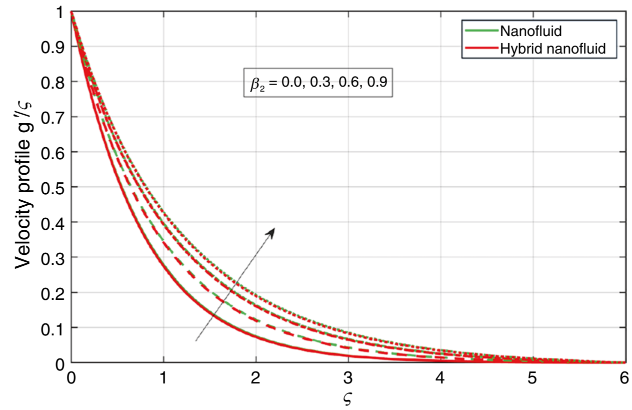

Fig. 6 Velocity distribution $g'(\eta)$ for variable viscosity β_2

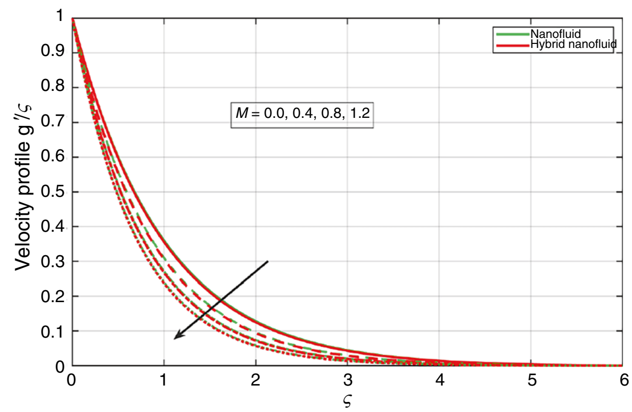

Fig. 7 The impacts of M impacts on $g'(\zeta)$

Temperature profiles

Figures 10–21 illustrate the impact of Prandtl number Pr, magnetic parameter M, thermal stratified parameter St parameters, stretching index m and thermal radiation parameter R, variable thermal conductivity λ_1, and thermal relaxation parameters λ_1 on temperature profile.

Figure 10 illustrates the effect of the Prandtl number Pr on the temperature field for Fe_3O_4 and TiO_2 nanoparticles. It is observed that the temperature profile $\theta(\eta)$ decreases with increasing Pr. Physically, increasing values of Pr would give rise to decreasing thermal diffusivity, restricting the diffusion of heat into the fluid. As a result, the thermal boundary layer becomes thinner, leading to a reduction in the temperature distribution.

Figure 11 shows the impacts of the magnetic field M on the temperature field for both TiO_2 and Fe_3O_4-based nanofluids. It is evident that the temperature profile $\theta(\zeta)$ decreased as the value of M increased. The decrease in temperature with increasing magnetic parameter M is due to the Lorentz

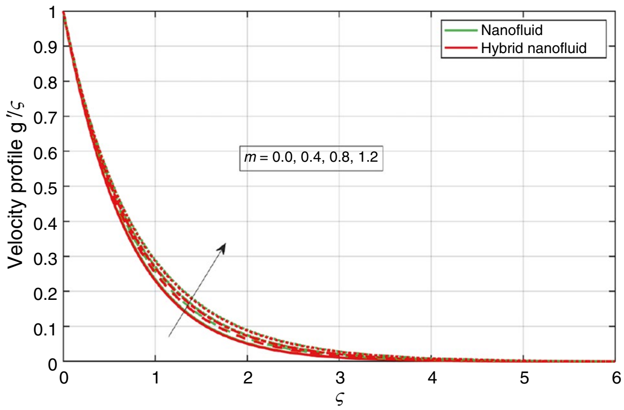

Fig. 8 The impact of stretching index m on $g'(\zeta)$

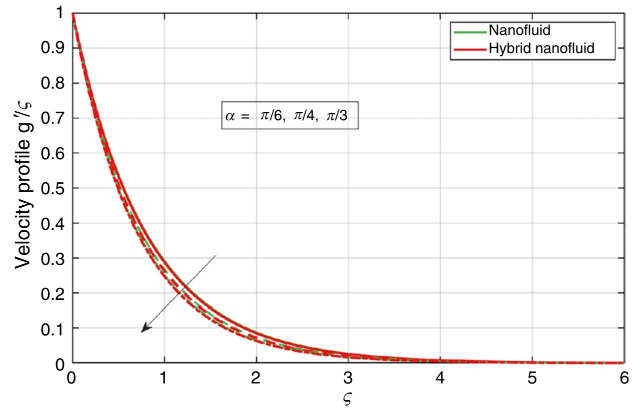

Fig. 9 An inclination angle α_1 on velocity field $g'(\zeta)$

force, which suppresses fluid motion and weakens convective heat transfer, resulting in a thinner thermal boundary layer.

Figures 12 and 13 illustrate the effect of the heat source parameters Q_1 and Q_2 on the temperature distribution of the Fe_3O_4–TiO_2 hybrid nanofluid. It is observed that the temperature increases with increasing values of both Q_1 and Q_2. Physically, an increase in the parameters of the higher heat source increases the internal heat generation in the fluid, which increases the thermal energy. This leads to an increase in the temperature field and a thickening of the thermal boundary layer.

Figure 14 illustrates the impacts of thermal radiation parameter R on temperature field $\theta(\eta)$ using the Fe_3O_4-TiO_2 hybrid nanofluid. The temperature profile enhances significantly as R increases. Physically, a higher R enhances the radiative heat transfer, providing extra energy to the fluid particles. In physical terms, the greater the value of R, the higher is the rate of radiative heat transfer resulting in the provision of more thermal energy to the fluid particles.

Figure 15 presents the effect of the convective boundary condition parameter B_1 on the temperature distribution $\theta(\eta)$ of the Fe_3O_4-TiO_2 hybrid nanofluid. The temperature profile increased with B_1 increases. Physically, the higher the values of B_1, the better the convective transfer of heat at the surface and the higher the amount of heat that is captured by the nanofluid. This produces a more viscous thermal boundary layer and increases the temperature distribution within the flow field. In turn an increase in the surface convection significantly increases the thermal energy of the fluid.

Figure 16 illustrates the effect of the thermal stratification parameter St on the temperature profile $\theta(\eta)$ for both TiO_2 and Fe_3O_4 nanofluids. It is observed that the temperature decreases significantly with increasing St. In physical terms, an increase in St is a sign of increased thermal stratification, with the temperature of the ambient fluid rising further away from the surface. This minimizes the difference in temperature between the wall and the fluid and thus undermines heat transfer and causes a drop in temperature distribution in the flow domain.

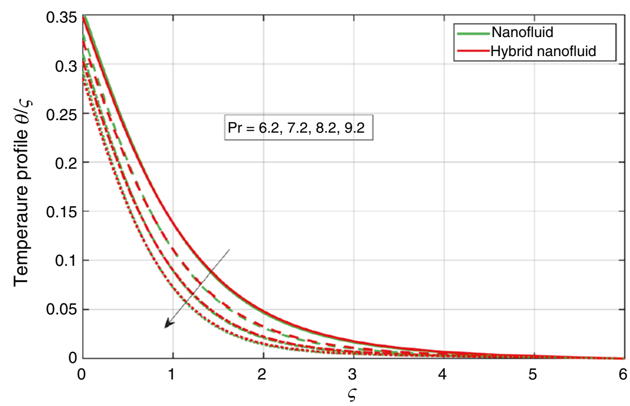

Fig. 10 Prandtl number Pr impacts on $\theta(\eta)$

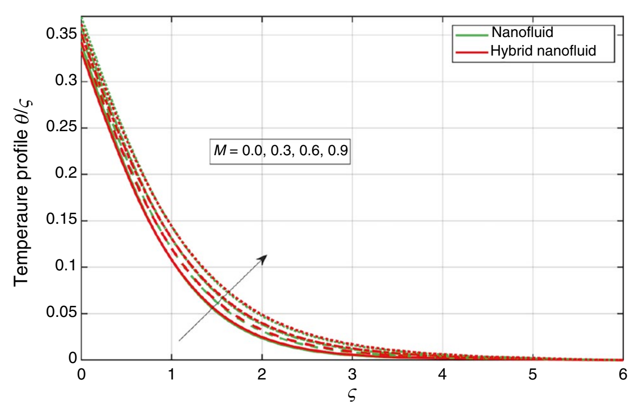

Fig. 11 The impacts of M on $\theta(\eta)$

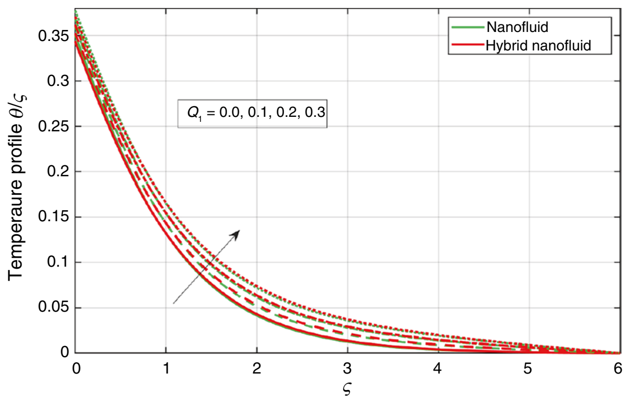

Fig. 12 The space-dependent heat source Q_1 impacts on temperature variation $\theta(\eta)$

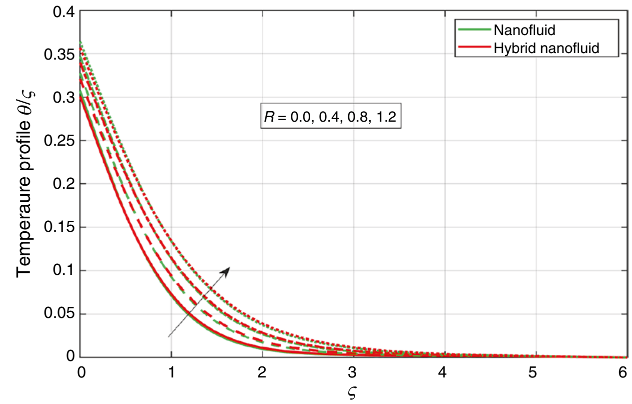

Fig. 14 Thermal radiation R impact on temperature distribution $\theta(\eta)$

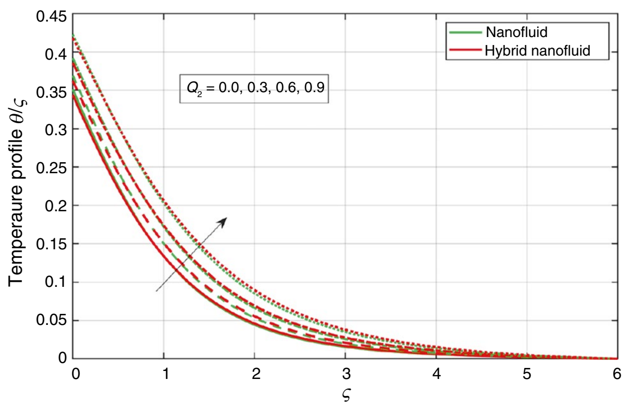

Fig. 13 Heat source parameter Q_2 impacts on $\theta(\eta)$

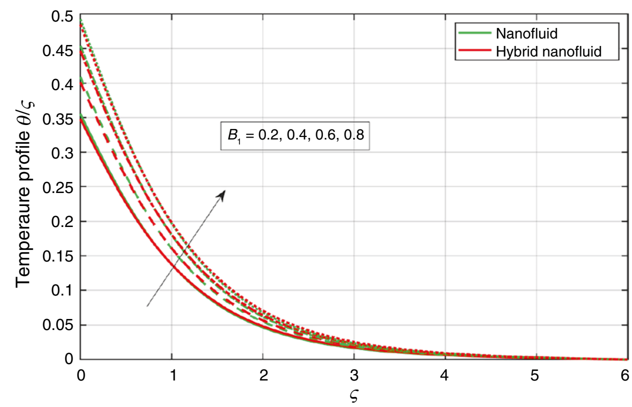

Fig. 15 Temperature variation $\theta(\eta)$ for heat convective parameter B_1

Figure 17 displays the temperature field with respect to (thermal relaxation λ_2) for (magnetic iron oxide Fe_3O_4 and titania oxide TiO_2). It is revealed that the temperature field decreased with an increases in λ_2. Physically, a larger thermal relaxation parameter will enable relaxation to transfer more heat between neighboring fluid particles, pending the thermal response, and decreasing the fluid temperature.

Figure 18 shows the impact of stretching index m, on the temperature variation of titanium(IV) oxide (TiO_2)–(Fe_3O_4). It was observed that decrease in the temperature field thereby increases the stretching index. Physically, the increased stretching index enhances the nonlinear stretching of the surface which accelerates the flow of the fluid and inhibits the growth of the thermal boundary layer, thereby lowering the temperature of the fluid.

The influence of the variable thermal conductivity parameter λ_1 on the temperature distribution $\theta(\eta)$ is illustrated in Fig. 19. It is observed that the temperature profile increases with increasing values of λ_1. Physically, an increase in the value of λ_1 increases the effective thermal conductivity of the fluid which helps increase diffusion of heat in the boundary layer. As a result, more thermal energy is transported away from the surface into the fluid, leading to an elevation in the temperature field. Consequently, the thermal boundary layer thickness increases with λ_1, indicating a stronger thermal diffusion effect in the fluid.

Figure 20 illustrates the effect of nanoparticle volume fractions (ϕ_1, ϕ_2) on the velocity profile $g'(\zeta)$. It is observed that the velocity decreases with increasing volume fractions of both nanoparticles. Physically, increasing concentrations of nanoparticles increase the effective viscosity of TiO_2 and Fe_3O_4 nanofluids resulting in an increase in the resistance to flow and, therefore, a reduction in fluid motion resulting in a thicker momentum boundary layer.

Figure 21 illustrates the effect of equal nanoparticle volume fractions $(\phi_1 = \phi_2)$ on the temperature profile $\theta(\zeta)$ for the hybrid nanofluid. It is observed that the temperature increases with increasing nanoparticle concentration. Physically, nanoparticles increase the effective thermal conductivity of the base fluid that boosts the heat transfer and increases temperature distribution in the thermal boundary layer of both TiO_2 and Fe_3O_4.

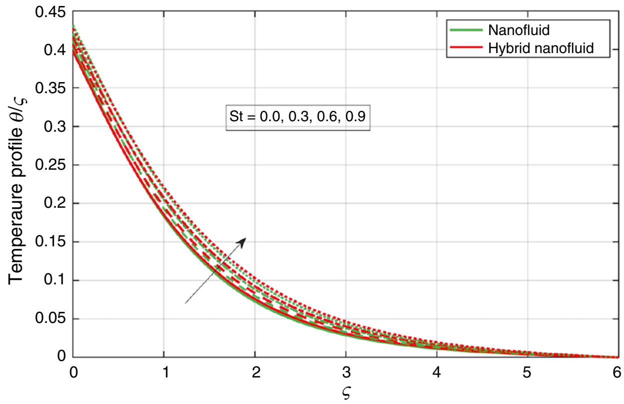

Fig. 16 Thermal stratification *St* effects on $\theta(\eta)$

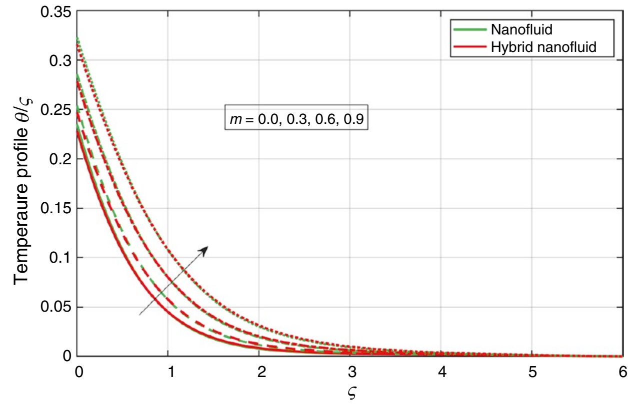

Fig. 18 The stretching index parameter m on $\theta(\eta)$

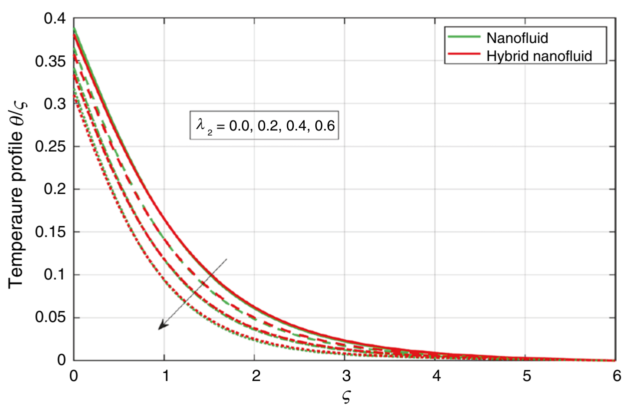

Fig. 17 The effects of λ_2 on $\theta(\eta)$

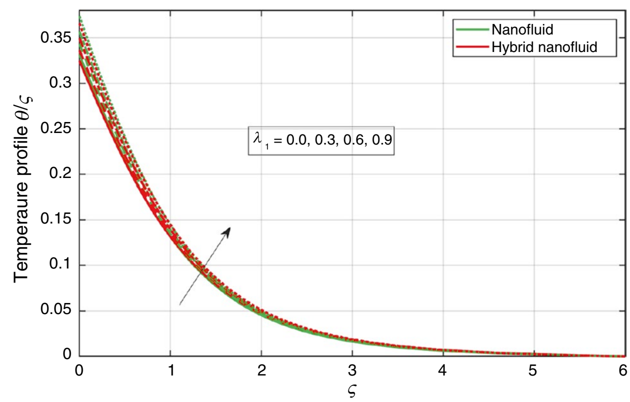

Fig. 19 The variable thermal conductivity λ_1 on $\theta(\eta)$

Skin friction coefficient and Nusselt number behavior

The influence of the governing physical parameters on the skin friction coefficient and Nusselt number is illustrated in Figs. 22–24. These values give a comparative study of nanofluid and hybrid nanofluid system in different thermal and flow conditions.

The variation of the Nusselt number with the Prandtl number for different values of the radiation parameter R is shown in Fig. 22. It is observed that the heat transfer rate increases with increasing Pr due to the reduction in thermal diffusivity, which leads to a thinner thermal boundary layer. Moreover, an increase in the value of R also increases the Nusselt number because thermal radiation increases the transport of energy. The fact that such a small difference occurred between nanofluid and hybrid nanofluid shows that the interactions between nanoparticles play a role in determining thermal behavior.

Figure 23 illustrates the variation of the skin friction coefficient with the stretching index m for different magnetic parameter values. The skin friction decreases with increasing m due to the reduction in velocity gradient at the wall caused by stronger stretching. However, increasing M enhances the magnitude of the skin friction coefficient due to the resistive Lorentz force. The hybrid nanofluid exhibits higher shear resistance compared to the nanofluid.

The variation of the Nusselt number with the stretching index m for different magnetic parameter values is depicted in Fig. 24. It is observed that the heat transfer rate decreases with increasing m due to the thickening of the thermal boundary layer. Further, the increase in the strength of the magnetic field decreases the Nusselt number because the Lorentz force will inhibit the convective heat transfer. The nanofluid shows slightly better thermal performance compared to the hybrid nanofluid.

Table 6 presents the variation of the skin friction coefficient C_f for both hybrid nanofluid and nanofluid under different physical parameters. It is observed that increasing the stretching parameter m reduces the magnitude of C_f, indicating a decrease in wall shear stress due to enhanced flow acceleration. The effect of a rise in the magnetic parameter, M, tends to raise the resistance to flow, and hence the shear

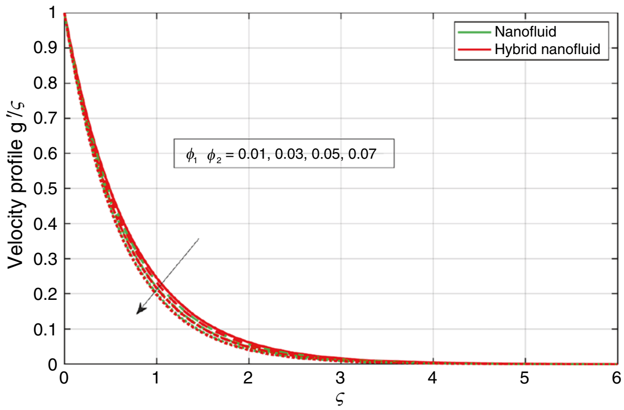

Fig. 20 The volume fraction $\phi_1 = \phi_2$ impacts on velocity $g'(\zeta)$

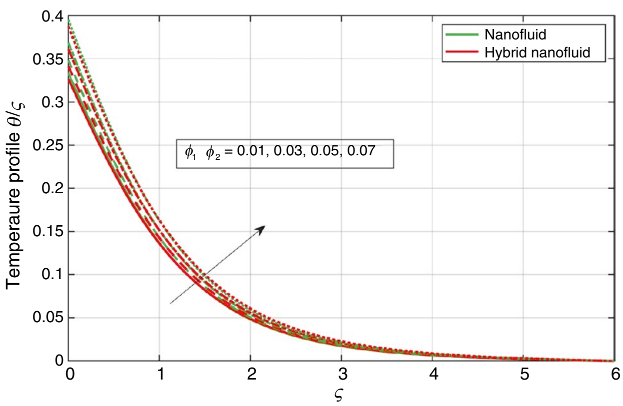

Fig. 21 Temperature influence for $\phi_1 = \phi_2$

effects, while changes in the nanoparticle volume fraction ($\phi1, \phi2$) are important in changing the effective viscosity and thus the wall drag. Overall, the hybrid nanofluid exhibits distinct behavior compared to the single nanofluid due to the combined influence of dual nanoparticles on fluid properties.

Table 7 illustrates the influence of various physical parameters on the Nusselt number for both hybrid nanofluid and nanofluid. It is evident that increasing the Prandtl number Pr enhances the heat transfer rate due to the thinning of the thermal boundary layer. The thermal radiation value, R, is inclined to decrease the Nusselt number, which indicates more thermal energy in the fluid. Additionally, parameters such as the heat source terms (Q_1, Q_2), and convective parameter B_1 significantly influence thermal transport, while the hybrid nanofluid demonstrates slightly altered heat transfer characteristics compared to the nanofluid due to improved effective thermal properties.

A comparison of the numerical analysis and ANN computation for hybrid nanoparticles is presented in Table 8. The good

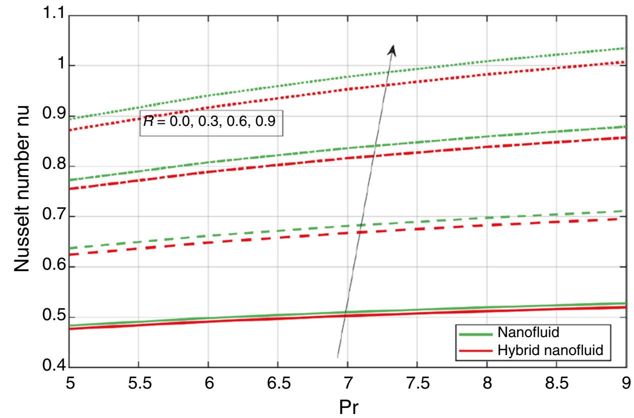

Fig. 22 Variation of the Nusselt number Nu with the Prandtl number Pr for thermal radiation parameter R

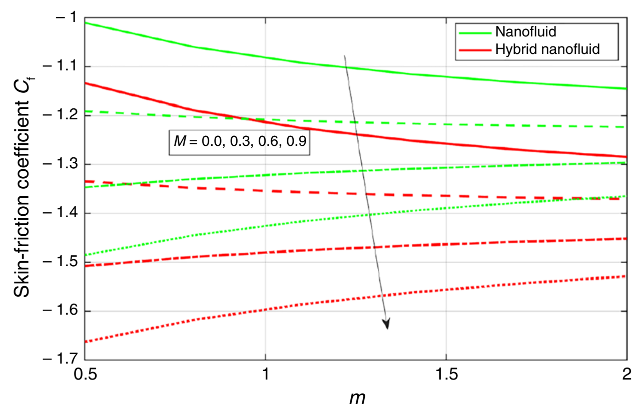

Fig. 23 Variation of the skin friction coefficient C_f with the stretching index m for magnetic parameter M

accuracy between both simulation was evaluated to ensure the validation of the model. Table1 shows the manner in which the coefficient of skin friction varies with the effects of the thermally

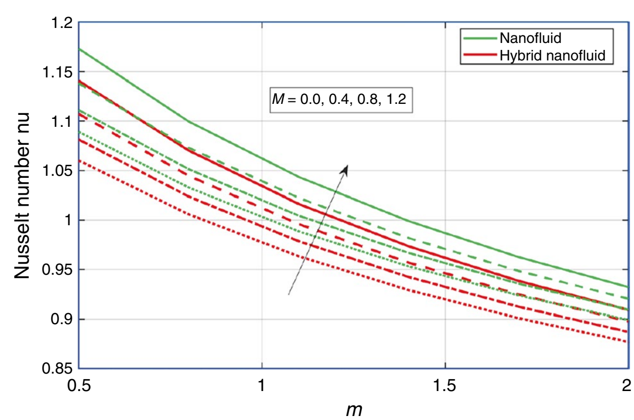

Fig. 24 Variation of the Nusselt number Nu with the stretching index m for magnetic parameter M

Table 6 The impacts of different parameters on C_f for hybrid nanoparticles

m	S_t	$\Bumpeq_3$	M	ϕ_1, ϕ_2	α_1	$f''(0)$ TiO_2-Fe_3O_4	$f''(0)$ TiO_2
0.5	0.1	0.01	2.0	0.04	90	−1.99154	−2.98423
	0.3					−2.01812	−2.07116
	0.5					−2.04508	−2.94167
0.1	0.4	0.01	2.0	0.04	90	−1.23387	−2.32021
0.4						−1.19876	−2.12408
0.7						−1.07121	−1.82413
0.5	0.4	0.01	0.1	0.04	90	−1.84865	−2.12906
			0.6			−1.17843	−2.68264
			1.1			−1.48281	−1.14632
0.1	0.4	0.02	2.0	0.04	90	−1.77804	−1.59836
		0.03				−1.65237	−1.67374
		0.05				−1.80902	−1.64664
0.1	0.4	0.01	2.0	0.01	90	−1.65861	−1.63801
				0.03		−1.76757	−1.68521
				0.05		−1.90672	−1.73556
0.1	0.4	0.04	2.0	0.30	30	−1.99156	−2.39716
					60	−1.05877	−1.51189
					90	−2.01065	−1.06519

Table 7 The impacts of different parameters on Nusselt number for both hybrid nanoparticles

S_t	Pr	B_1	R	m	M	λ_2	Q_2	Q_1	ϕ_1, ϕ_2	$\theta'(0)$ TiO_2-Fe_3O_4	$\theta'(0)$ TiO_2
0.1	6.3	0.4	2.0	0.5	2.0	0.1	1.0	1.0	0.04	−1.63268	−1.84845
0.3										−1.63127	−1.93239
0.5										−1.62986	−2.01862
0.4	6.3	0.3	2.0	0.5	2.0	0.1	1.0	1.0	0.04	−0.77743	−0.77422
		0.5								−1.37687	−1.36782
		0.7								−1.86075	−1.84484
0.4	7.4	0.4	2.0	0.5	2.0	0.1	1.0	1.0	0.04	−1.41074	−1.40211
	8.4									−1.43491	−1.43059
	9.4									−1.45908	−1.45487
0.4	6.3	0.4	2.0	0.1	1.5	0.1	1.0	1.0	0.04	−2.12408	−1.59465
				0.4						−1.90809	−1.41553
				0.7						−1.77098	−1.28091
0.4	6.3	0.4	0.1	0.5	1.5	0.1	1.0	1.0	0.04	−1.36941	−1.36027
			0.6							−1.35917	−1.34315
			1.1							−1.34475	−1.33567
			1.6							−1.33033	−1.32119

Table 8 The compression of (numerical and ANN) results for simple and hybrid nanoparticles

M	Simple nanoparticles		Hybrid nanoparticles	
	Numerical result	ANN result	Numerical result	ANN result
0.2	−0.776391063	−0.768702106	−0.952191637	−0.951951184
0.4	−0.735274009	−0.813909181	−1.008203164	−1.007940483
0.6	−0.774229942	−0.857235546	−1.061619298	−1.061367706
0.8	−0.811517269	−0.898318815	−1.112747448	−1.112433812

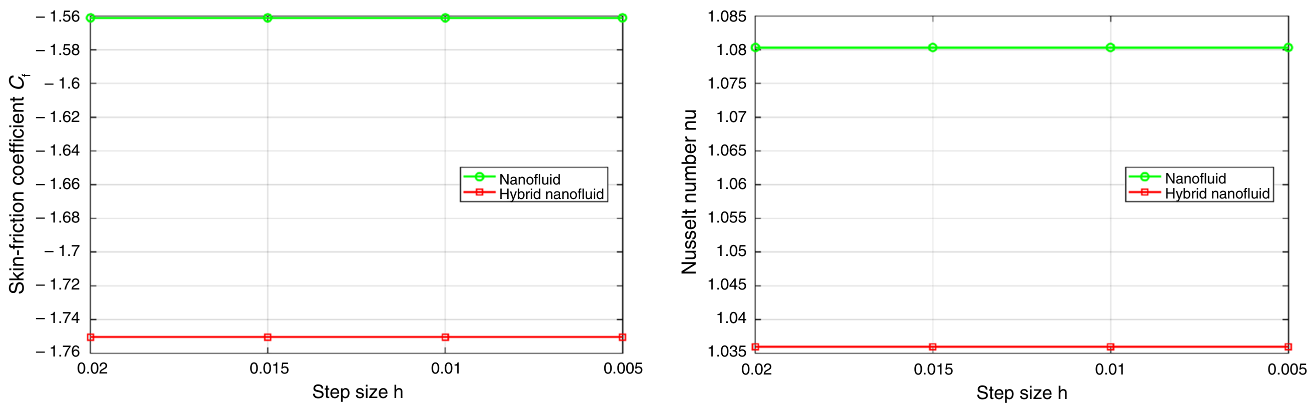

Fig. 25 Grid independence of C_f and Nu for nanofluid and hybrid nanofluid

stratified St, inclination angle α_1, stretching index m, and magnetic parameter M. This indicates that the friction coefficient between the skin increases with a higher values of , St, M, α_1 and m for the nanofluids made of Fe_3O_4 and TiO_2. However, on the other hand, the skin friction coefficient declines with an rise in the wall thickness parameter ß$_3$.

The grid independence study for both nanofluid and hybrid nanofluid cases is presented in Fig. 25a and b, where the variation of the skin friction coefficient C_f and Nusselt number Nu is examined for different step sizes $h = 0.02$, 0.015, 0.01, and 0.005. It is apparent that both Cf and Nu do not vary much when the grid is refined, and this means that they are insensitive to the step size. The variation in the computed values is extremely small, confirming that the numerical solution is independent of the grid resolution.

Conclusions

This study investigated the thermal stratified flow of a hybrid nanofluid comprising titanium(IV) oxide (TiO_2) and magnetite ($Fe_3\ O_4$)/H_O across a nonlinear stretchable surface. In addition, in this mathematical model the temperature dependence of both thermal conductivity and viscosity and an inclined magnetic field are presented. The governing fluid model was recast into a coupled nonlinear ODEs system which is numerically solved using with shooting method combined with artificial neural network (ANN) method. The consequences of velocity and energy field were studied and graphically represented. The heat transfer rate and drag coefficient were determined and tabulated for the different physical parameters. The study demonstrates that hybrid nanofluids significantly enhance heat transfer compared to conventional nanofluids. The ANN model achieved high accuracy with RMSE of order 10^{-4}. The principal findings are summarized as follows:

- The velocity profile reduces with the wall thickness parameter(s) ≎$_3$, variable viscosity parameter ≎$_2$, stretching index (m), magnetic parameter M, inclination angle (α_1), and nanoparticle volume fractions. These are the effects that are related to the viscous resistance that is enhanced, the magnetic damping that is stronger, and the opposition to the flow that is augmented near the wall.
- This is because the temperature profile rises with rising radiation parameter, convective parameter, and heat source parameters, as these parameters raise the thermal energy available to the fluid.
- The temperature profile will have a tendency to decreasing as the Prandtl number (Pr) and the thermal stratification parameter (St) and the thermal relaxation parameter λ_2 and the index of stretching (m) increase, and this implies less thermal diffusion and less strong thermal boundary layer generation.
- The ANN predictions were in good agreement with the numerical results, and it indicates that the trained ANN can be effectively used as a surrogate of this type of coupled nonlinear transport problems.
- The hybridized numerical-ANN model shows viable possibilities of designing and optimizing thermal systems with hybrid nanofluids, and specifically, heat transfer equipment, solar energy equipment, cooling equipment, and sophisticated heat transfer equipment.

This study demonstrates the effectiveness of combining numerical and machine learning approaches for complex thermal systems. The framework developed could be applied to turbulent flows, experimental validation, and optimization-based thermal system design.

Acknowledgements The author M. Alqudah acknowledged Princess Nourah bint Abdulrahman University Researchers Supporting Project number (PNURSP2026R14), Princess Nourah bint Abdulrahman University, Riyadh, Saudi Arabia. Also, authors are thankful to Prince Sultan University for support through TAS research lab.

Author contributions HZ and KS prepared the draft and conducted a formal analysis. MBJ edited the manuscript and explained the numerical analysis. ZA included a software procedure and numerical treatment. TA supervised the project and conducted the investigation. MA and AM included a numerical analysis and methodology

Funding Open access funding provided by the Scientific and Technological Research Council of Türkiye (TÜBİTAK). We authors declare that there is no external funding source available this time.

Data availability No datasets were generated or analyzed during the current study.

Declarations

Competing interests The authors declare no competing interests.

References

1. Choi SU, Eastman JA, Enhancing thermal conductivity of fluids with nanoparticles, Argonne National Lab. (ANL), Argonne, IL, USA.
2. Zeb H, Wahab HA, Khan U, Ehab M, Malik MY. The modified heat flux modeling in nanoparticles (Fe3O4 and aggregation nanoparticle) based fluid between two rotating disks. Energies. 2022;15(11):4088.
3. Obalalu A, Darvesh A, Aselebe L, Salawu S, Issa K. Thermal management of radiation mechanism over a stretchable curved surface inside the circle: performance enhancement of molybdenum disulfide and silicon dioxide hybrid nanofluid for thermal technology advancement. Int J Ambient Energy. 2024;45(1):2354505.
4. Bhatti M, Öztop HF, Ellahi R, Sarris IE, Doranehgard MH. Insight into the investigation of diamond (C) and silica (SiO2) nanoparticles suspended in water-based hybrid nanofluid with application in solar collector. J Mol Liq. 2022;357:119134.
5. Nabwey HA, Khan WA, Rashad AM, Abdelrahman ZM, Hawsah MA. Thermodynamic analysis of mixed convective ternary-hybrid Ree-Eyring nanofluid flow past a static wedge. Spec Top Rev Porous Media Int J. 2025;16(2):25–57.
6. Nabwey HA, Khan WA, Rashad AM, Elmeky H, Abdelnaem S, Hawsah MA. Solar energy improvement in solar HVAC using Sutterby magneto-ternary hybrid nanofluid flow with Moluchowski temperature conditions: a solar thermal application. ZAMM J Appl Math Mech. 2023;103(10):e202300063.
7. Zeb H, Munir T, Zaman M, Malik M. Analysis of melting heat transfer in ternary nanofluid flow between rotating disks with non-linear thermal radiation. Results Eng. 2025;25:104383.
8. Zeb H, Shah K, Alqudah M, Abdeljawad T. Variable thermal conductivity effects on MHD flow of non-Newtonian ternary hybrid nanofluid between rotating disks: a Cattaneo-Christov heat transfer analysis. Case Stud Therm Eng. 2025;71:106119.
9. Bar N, Biswas MN, Das SK. Prediction of pressure drop using artificial neural network for gas non-Newtonian liquid flow through piping components. Ind Eng Chem Res. 2010;49(19):9423–9.
10. Zhao T-H, Khan MI, Chu Y-M. Artificial neural networking (ANN) analysis for heat and entropy generation in flow of non-Newtonian fluid between two rotating disks. Math Methods Appl Sci. 2023;46(3):3012–30.
11. Alizadeh R, Mesgarpour M, Ameri A, Abad JMN, Wongwises S. Artificial intelligence prediction of natural convection of heat in an oscillating cavity filled by CuO nanofluid. J Taiwan Inst Chem Eng. 2021;124:75–90.
12. Yu WS, Dwyer OE. Heat transfer to liquid metals flowing turbulently in eccentric annuli—I. Nucl Sci Eng. 1966;24(2):105–117.
13. Cattaneo C. Sulla conduzione del calore Attidel Seminario Matematico e Fisicodella. Università di Modena. 1948;3:1948–9.
14. Christov C. On frame indifferent formulation of the Maxwell–Cattaneo model of finite-speed heat conduction. Mech Res Commun. 2009;36(4):481–6.
15. Wang C, Liu X, Zhao M. Thermal relaxation effects in ultrafast laser heating. Int J Therm Sci. 2023;185:108–20.
16. Ali M, Rahman S, Hussein A. Hyperbolic heat conduction in modern electronic devices. J Electron Packag. 2024;146(3):031001.
17. Chen L, Wang J. Bioheat transfer with memory effects: applications in thermal therapy. Int J Heat Mass Transf. 2024;195:123–34.
18. Rao V, Thompson D. Microscale heat transfer: from phonons to continuum. Ann Rev Heat Transf. 2025;28:45–78.
19. Daniel YS, Aziz ZA, Ismail Z, Salah F. Thermal stratification effects on MHD radiative flow of nanofluid over nonlinear stretching sheet with variable thickness. J Comput Design Eng. 2018;5(2):232–42.
20. Nadeem S, Ishtiaq B, Alzabut J, Ghazwani HA. Entropy generation for exact irreversibility analysis in the MHD channel flow of Williamson fluid with combined convective-radiative boundary conditions. Heliyon. 2024;10(4):e26432.
21. Chen C, Eichhorn R. Natural convection from a vertical surface to a thermally stratified fluid. J Heat Transf. 1976;98(3):446–51.
22. Singh R, Gupta P, Sharma A. Optimization of thermally stratified energy storage systems. Renew Energy. 2023;210:245–58.
23. Gupta S, Reddy K. Solar ponds with enhanced stratification for power generation. Sol Energy. 2024;268:112–25.
24. Khan U, Zaib A, Ishak A. Dual stratified nanofluid flow over an exponentially stretching sheet. Chin J Phys. 2024;89:412–25.
25. Ahmed N, Sheikholeslami M. Double stratification in magnetohydrodynamic Casson nanofluid flow. Int Commun Heat Mass Transf. 2025;135:107–18.
26. Rodriguez P, Martinez F. Phase change materials with thermal relaxation effects. Energy Storage Mater. 2025;65:103–15.
27. Kim H, Lee J, Choi M. Thermal performance of microchannel heat sinks with stratified two-phase flow. Appl Therm Eng. 2023;225:120–32.
28. Taylor R, Johnson M. Electronic cooling using dielectric stratified flows. IEEE Trans Compon. 2024;14(2):345–56.
29. Ramesh NA, Tripathi D. Experimental investigation and linear modeling of temperature-dependent thermal conductivity in hybrid nanofluids for solar thermal applications. Int J Therm Sci. 2024;201:108–19.
30. Chiam TC. Heat transfer with variable thermal conductivity in a stagnation-point flow towards a stretching sheet. Int Commun Heat Mass Transf. 1996;23(2):239–48. https://doi.org/10.1016/0735-1933(96)00004-7.
31. Chen X, Li W. PIV-based experimental analysis of temperature-dependent viscosity effects on vortex dynamics in MHD natural convection. Exp Therm Fluid Sci. 2025;158:111–23.
32. Molla MM, Hossain MA, Yao L-S. Natural convection flow from an isothermal sphere with temperature-dependent viscosity. Int J Therm Sci. 2005;44(9):910–8. https://doi.org/10.1016/j.ijthermalsci.2005.02.012.

33. Kumar CM, Park SH. A coupled CFD-chemical kinetics model for laminar reactive flows with temperature-dependent transport properties. Int Commun Heat Mass Transf. 2024;155:107–18.
34. Ghaly AY, Seddeek MA. Effects of variable viscosity and thermal conductivity on MHD flow and heat transfer along a semi-infinite horizontal plate. J Magn Magnetic Mater. 2004;270(1–2):130–8. https://doi.org/10.1016/j.jmmm.2003.08.012.
35. Mackolil J, Mahanthesh B. Inclined magnetic field and nanoparticle aggregation effects on thermal Marangoni convection in nanoliquid: a sensitivity analysis. Chin J Phys. 2021;69:24–37.
36. Khan M, Salahuddin T, Malik M, Mallawi FO. Change in viscosity of Williamson nanofluid flow due to thermal and solutal stratification. Int J Heat Mass Transf. 2018;126:941–8.
37. Khan N, Shaheen A, Abbas N, Siddique I, Shatanawi W. Effects of MHD and thermal radiation on non-Newtonian fluid with Cattaneo–Christov heat over a stretching flow surface. Numer Heat Transf Part A Appl. 2025;86(15):5206–21.
38. Animasaun I, Ajayi T, Omowaye J. Effects of viscous dissipation and double stratification on MHD Casson fluid flow over a surface with variable thickness: boundary layer analysis. Int J Eng Res Afr. 2017;28:73–89. https://doi.org/10.4028/www.scientific.net/JERA.28.73.
39. Daniel YS, Aziz ZA, Ismail Z, Salah F. Double stratification effects on unsteady electrical MHD mixed convection flow of nanofluid with viscous dissipation and joule heating. J Appl Res Technol. 2017;15(5):464–76. https://doi.org/10.1016/j.jart.2017.05.007.
40. Esfandiari RS. Numerical methods for engineers and scientists using MATLAB. Boca Raton: CRC Press; 2013.
41. Kumari P, et al. Inclined MHD hybrid nanofluid flow with nonlinear radiation over a stretching surface. Symmetry. 2025;17(8):1330.
42. Hussain A, Malik M, Awais M, Salahuddin T, Bilal S. Computational and physical aspects of MHD Prandtl-Eyring fluid flow analysis over a stretching sheet. Neural Comput Appl. 2019;31(Suppl 1):425–33.
43. Abbas N, Shatanawi W. Numerical investigation of time-dependent MHD rotating hybrid nanofluid flow over a permeable stretching sheet. Modern Phys Lett B. 2024;38(35):2450324.
44. Zeb H, Bhatti S, Khan U, Wahab HA, Munir T, Malik M. Cattaneo–Christov heat flux modeling in nanofluid TiO2–Titanium oxide and aggregation nanoparticle flow between two rotating disks. Waves Random Complex Media 2023; 1–21.
45. Maatki C, Khan SU, Selimefendigil F, Kolsi L. Artificial neural network-guided heat transfer analysis of tri-hybrid nanofluid thin film flow under realistic thermal constraints: advanced energy applications. Case Stud Therm Eng. 2025;74:106975.
46. Wahab HA. A numerical approach of slip conditions effect on nanofluid flow over a stretching sheet under heating joule effect. Punjab Univ J Math. 2025;51(5):79–95.
47. Awan AU, Niazai S, Hussain M, et al. Entropy optimization in MHD hybrid nanofluid flow over a stretching sheet. Sci Rep. 2025;15:38931.